TECHNICAL MEMORANDUM

X-361

WIND-TUNNEL INVESTIGATION OF THE STATIC AND DYNAMIC-ROTARY STABILITY DERIVATIVES OF A FLAT-TOP WING-BODY MODEL AT MACH NUMBERS OF 2.5, 3.0, AND 3.5

By Bedford A. Lampkin and Kenneth C. Endicott

Ames Research Center
Moffett Field, Calif.

NATIONAL AERONAUTICS AND SPACE ADMINISTRATION

WASHINGTON

April 1960

NATIONAL AERONAUTICS AND SPACE ADMINISTRATION

TECHNICAL MEMORANDUM X-361

WIND-TUNNEL INVESTIGATION OF THE STATIC AND DYNAMIC-ROTARY STABILITY DERIVATIVES OF A FLAT-TOP WING-BODY MODEL AT MACH NUMBERS OF 2.5, 3.0, AND 3.5*

By Bedford A. Lampkin and Kenneth C. Endicott

SUMMARY

The results of a wind-tunnel investigation of the static and dynamic-rotary stability derivatives for a flat-top wing-body model are presented. The test was conducted at Mach numbers of 2.5, 3.0, and 3.5, and a Reynolds number of 5 million. The angle-of-attack range was approximately -16° to $+12^\circ$ at 0° sideslip. Also, static data were obtained through the angle-of-attack range at a constant 5° angle of sideslip and within an angle-of-sideslip range of -10° to $+6^\circ$ at a constant angle of attack of 6°.

The model consisted of an arrow wing with tips drooped along a line inclined 3° to the model plane of symmetry, and a 3/4-power ogive half body mounted beneath the wing. A ventral fin was located at the rear of the half body.

It was found that the model was directionally unstable at positive angles of attack above 5°; however, the dynamic damping was stabilizing about the three body axes throughout the test range. With either elevon or rudder deflection there were pronounced cross-coupling effects on the lateral and directional stability of the aircraft which make proper roll control difficult to attain. Finally, elementary methods of estimating the derivatives were only moderately successful.

*Title, Unclassified

INTRODUCTION

Several analytical and wind-tunnel studies have considered the possibility of obtaining high lift to drag ratios on flat-top configurations as a result of beneficial aerodynamic interference effects (refs. 1, 2, and 3). The model of this investigation evolved from these studies.

The problems of designing practical aircraft for flight at hypersonic speeds are further complicated because stability and control must be maintained over large speed ranges. The primary purpose of this report is to supply data for analyzing the stability and control of the test configuration. Also, an assessment is made of the current methods of predicting the dynamic stability derivatives by comparing estimated values with experimental results.

With the model mounted on a six-component strain-gage balance, the following aerodynamic coefficients were obtained: lift, drag, pitching moment, side force, yawing moment, and rolling moment. During a second phase of the test, the model was mounted on a dynamic balance and the following stability derivatives were obtained: pitching moment due to angle of attack, damping in pitch, yawing moment due to angle of sideslip, damping in yaw, rolling moment due to yawing velocity, damping in roll, and yawing moment due to rolling velocity.

SYMBOLS

The aerodynamic coefficients and stability derivatives defined in this section are oriented about a body system of axes as shown in figure 1. The angular dimensions are degrees and radians for the static and dynamic derivatives, respectively. The location of the model moment center was at 76 percent of the body length aft of the nose which corresponds to 55.4 percent of the wing mean aerodynamic chord.

C_L lift coefficient, $\dfrac{\text{lift}}{\frac{1}{2}\rho V^2 S}$

C_D drag coefficient, $\dfrac{\text{drag}}{\frac{1}{2}\rho V^2 S}$

C_m pitching-moment coefficient, $\dfrac{\text{pitching moment}}{\frac{1}{2}\rho V^2 S\bar{c}}$

C_Y side-force coefficient, $\dfrac{\text{side force}}{\frac{1}{2}\rho V^2 S}$

C_n yawing-moment coefficient, $\frac{\text{yawing moment}}{\frac{1}{2}\rho V^2 Sb}$

C_l rolling-moment coefficient, $\frac{\text{rolling moment}}{\frac{1}{2}\rho V^2 Sb}$

C_{m_α} $\frac{\partial C_m}{\partial \alpha}$

C_{m_q} $\frac{\partial C_m}{\partial (q\bar{c}/2V)}$

$C_{m_{\dot{\alpha}}}$ $\frac{\partial C_m}{\partial (\dot{\alpha}\bar{c}/2V)}$

C_{n_β} $\frac{\partial C_n}{\partial \beta}$

C_{n_r} $\frac{\partial C_n}{\partial (rb/2V)}$

$C_{n_{\dot{\beta}}}$ $\frac{\partial C_n}{\partial (\dot{\beta}b/2V)}$

C_{l_r} $\frac{\partial C_l}{\partial (rb/2V)}$

$C_{l_{\dot{\beta}}}$ $\frac{\partial C_l}{\partial (\dot{\beta}b/2V)}$

C_{l_p} $\frac{\partial C_l}{\partial (pb/2V)}$

C_{n_p} $\frac{\partial C_n}{\partial (pb/2V)}$

M Mach number

S wing area

V velocity

X,Y,Z system of body axes (see fig. 1)

b wing span

$\bar{c}$ wing mean aerodynamic chord

p	rotational velocity about X axis, radians/sec
q	rotational velocity about Y axis, radians/sec
r	rotational velocity about Z axis, radians/sec
$\frac{x}{l}$	fraction of fuselage length (see fig. 2)
α	angle of attack, radians except where noted
β	angle of sideslip, radians except where noted
δ	deflection angle, deg
ρ	density
Δ	increment

Subscripts

e	both elevons
e_L	left elevon
e_R	right elevon
R	rudder

MODEL

The model of this investigation consisted of a notched arrow wing with 45° drooped tips and a 3/4-power ogive half body (40 inches long with a 5-inch cylindrical extension) mounted beneath the wing. A ventral fin and rudder were attached to the aft underside of the fuselage. All model components were aluminum. Dimensions of the model are given in figure 2, and photographs of the model in the wind-tunnel test section are shown in figure 3.

APPARATUS

Tests were conducted in the 8- by 7-foot supersonic test section of the Ames Unitary Plan Wind Tunnel. This wind tunnel is capable of continuous variation of Mach number from 2.5 to 3.5 and of stagnation pressures from 2 to 28 psia. A more detailed description of the wind tunnel may be found in reference 4.

The static force data were measured on a six-component strain-gage balance. The signal output from the balance was processed through a digital computer to obtain the coefficients.

During a second phase of the test the model was mounted successively on two dynamic balances. These balances were free to oscillate about a single axis so that one balance could produce a rolling oscillation while the other, depending on its axis orientation, could produce either a yawing or pitching oscillation. Oscillation amplitudes were controlled by an electronic feedback system utilizing strain gages mounted in the balance. The strain-gage output signals were digitized and with the period of oscillation were processed through a digital computer to produce the dynamic stability derivatives.

Further information on the rotary derivatives testing technique and the associated equipment may be found in reference 5.

TESTS AND PROCEDURE

Tests of the flat-top configuration were conducted at Mach numbers of 2.5, 3.0, and 3.5 and at a Reynolds number of 5 million based on the mean aerodynamic chord.

Static force data were obtained within the range of angles of attack of -16° to $+12^\circ$ at constant angles of sideslip of both 0° and 5°, and within the range of angles of sideslip of -10° to $+6^\circ$ at a constant angle of attack of 6°. Elevon effects were determined with both elevons at 0°, $+20^\circ$, and -20° and with the left elevon only at these positions. The model was tested with the ventral fin undeflected and deflected 10°, and without the ventral fin.

Dynamic data were obtained through an angle-of-attack range of -16° to $+12^\circ$ and an angle of sideslip of 0°. Yawing and rolling oscillations were conducted with the elevons and the ventral fin undeflected. Additional tests were made without the ventral fin in place.

For the pitching oscillation tests the rudder remained undeflected and the elevons were deflected either 0°, $+10^\circ$, $+20^\circ$, or -10° to reduce the model static pitching moment at a given angle of attack as necessitated by the testing technique.

The range of oscillation amplitudes was between $\pm 1^\circ$ and $\pm 2^\circ$ at oscillation frequencies between 4 and 8 cycles per second. Data were generally taken at the maximum oscillation amplitude obtainable and again at an amplitude of approximately one half the former. The variation of the data for the two conditions was within the random scatter.

CORRECTIONS AND ACCURACY

Pressures were measured at the base of the model and applied to the static force data as a base drag correction which replaced the measured base pressures by free-stream static pressure.

For the dynamic balances, corrections to the measured values of the damping coefficients caused by mechanical damping of the oscillations were determined from wind-off measurements with the tunnel evacuated to a pressure of approximately 5 inches of mercury. The largest tare values were approximately 0.015 in derivative units.

The accuracy of the static data is listed in the following table. The figures are based on the mechanical and electrical repeatability of the recording equipment.

C_L	± 0.001	C_n	± 0.0003
C_D	± 0.0003	C_l	± 0.0003
C_m	± 0.0010	α	$\pm 0.2^\circ$
C_Y	± 0.001	β	$\pm 0.2^\circ$

The precision of the dynamic data is indicated on the data plots by a comparison of the data point value and the nominal value fairings of the plots.

RESULTS

Table I is an index of the results of the wind-tunnel tests presented in the figures.

DISCUSSION

In the discussion which follows, the static force data of figures 4, 5, 9, and 10 are mentioned only as they affect the discussion of the stability derivatives. The predicted derivative values are indicated by the broken lines on the appropriate figures and are based on methods which generally do not attempt to predict aerodynamic interference effects.

Static Longitudinal Characteristics

Static longitudinal stability.- In figure 6 the values of C_{m_α} indicate static stability in pitch at angles of attack more positive than approximately -5°. At greater negative angles of attack, the data indicate static instability in pitch.

Theoretical values of C_{m_α} were not derived because of the complex nature of the aerodynamic interference. Instead, the broken-line curves of C_{m_α} in figure 6 were obtained from static pitching-moment data with $\delta_e = 0^\circ$ and $+20^\circ$. The agreement between the two experimentally obtained derivatives is good. It is of interest to note the spread in the values of C_{m_α} at about -2° angle of attack, where C_{m_α} is highly influenced by the elevon setting.

Elevon pitch effectiveness.- In figure 7 values of $\Delta C_m/\Delta\delta_e$ versus angle of attack at the three Mach numbers are given. It is apparent that elevon pitch effectiveness does not remain constant with changes in angle of attack, and opposite elevon deflections produce opposite changes in magnitude of effectiveness with a change in angle of attack. Greater values of $\Delta C_m/\Delta\delta_e$ were obtained at large positive angles of attack than were obtained at large negative angles with equal but opposite elevon settings. Also, with the elevons deflected below the wing, the deflection of both elevons was generally more than twice as effective as the deflection of a single elevon.

Dynamic Longitudinal Characteristics

Damping in pitch.- Stabilizing damping in pitch was exhibited by the model at all Mach numbers and angles of attack (fig. 8). The mean value of damping decreased slightly as the Mach number increased.

The predicted values were in good agreement with the experimental results at the higher Mach numbers. The estimated values were obtained

from references 6 and 7 by subtracting the damping of the notched aft section from that of a triangular wing having an aspect ratio corrected for the drooped tip.

Static Lateral-Directional Characteristics

Static lateral stability.- Values of the effective dihedral derivative are given in figure 11(b) as incremental values of C_l for a 5° increment of sideslip angle. At positive angles of attack the model exhibited a positive dihedral effect which became negative below approximately -1° angle of attack. The ventral fin contributed a small negative dihedral effect at all test Mach numbers and angles of attack.

Rudder effectiveness.- In figure 12(b) the data indicate that the rudder effectiveness increases with increased angle of attack. Nearly the same rudder effect can be obtained from positive elevon deflection, while negative elevon deflections are more than twice as effective as the rudder (at negative angles of attack only) in producing yawing moment. This cross-coupling effect of the elevons results, of course, from the elevons being located on the deflected wing tips. A cross-coupling effect of the rudder is also noted in figure 12(a); namely that the rudder is capable of producing an appreciable rolling moment.

Elevon rolling effectiveness.- As was true of elevon pitch effectiveness the roll effectiveness changed with the direction of the elevon deflection. An elevon deflection below the wing was more effective in producing roll than a deflection above the wing when the model was at positive angle of attack. Elevon rolling effectiveness for elevon deflections above and below the wing (fig. 12(a)) appears to coincide at an angle of attack which increases with increased Mach number. It should be noted that because the elevons are attached to the drooped wing tips and act to some extent as rudders, attempts to roll the aircraft by elevon deflection produce unusually large yawing moments.

Static directional stability.- Without the ventral fin, the model possessed marginal or zero directional stability at zero angle of attack, and was unstable at positive angles of attack (fig. 13). The addition of the ventral fin to the model provided directional stability up to approximately 3° angle of attack.

The values of C_{n_β} in figure 13 were obtained with the dynamic balance. Values of C_{n_β} derived from the static balance data in figure 10 (the model being at 6° angle of attack only) agree reasonably well with those obtained with the dynamic balance. At zero and negative values of angle of attack, values of $\Delta C_n/\Delta\beta$ from figure 11(c) are also in

good agreement with the C_{n_β} values of figure 13, particularly at the lower Mach numbers. The differences between the curves of figures 13 and 11(c) at positive angles of attack are traceable to the "S" shape of the curves of C_n vs. β (see fig. 10(a) for example). The dynamic balance determines the derivative C_{n_β} near $\beta = 0$ where the curve of C_n vs. β is steep; whereas $\Delta C_n/\Delta\beta$ is based on an increment of C_n over a sideslip angle range of 5° where the rate of change of C_n is not as great. At the higher Mach numbers the curvature of the C_n vs. β curves is less and the agreement between the curves of figures 13 and 11(c) improves.

The estimated values shown in figure 13 as broken lines are the sum of the contribution from the fuselage (method of ref. 8) and the drooped tips, assuming the latter to have two-dimensional characteristics. At zero angle of attack these predicted values were in good agreement with the experimental results.

Dynamic Lateral-Directional Characteristics

Damping in yaw.- Stabilizing damping in yaw was displayed by the model at all Mach numbers and angles of attack (fig. 14). The ventral fin provided a nominal increase in the damping which varied between zero and approximately twice the estimated value. In this estimate the contribution of the body was obtained from equation (B_{21}) of reference 9, and a two-dimensional lift-curve slope was assumed for the drooped tips and ventral fin. The predicted values for the model were in fair agreement with the experimental data except for the highest angles of attack.

Rolling moment due to yawing velocity.- The complete model exhibited negative values of $C_{l_r} - C_{l_{\dot\beta}} \cos\alpha$ at all Mach numbers and angles of attack (fig. 15). The contribution of the ventral fin varied markedly with angle of attack and Mach number.

Values of $C_{l_r} - C_{l_{\dot\beta}} \cos\alpha$ predicted on the assumption that the drooped tips and ventral fins had two-dimensional lift-curve slopes were not in agreement with the data.

Damping in roll.- Stabilizing damping in roll was exhibited by the model at all Mach numbers and angles of attack (fig. 16). The ventral fin generally had a small but variable effect.

Predicted values obtained from reference 6 (for the projected wing aspect ratio) were in fair agreement with the experimental results at zero angle of attack.

Yawing moment due to rolling velocity.- Values of $C_{n_p} + C_{n_{\dot{\beta}}} \sin \alpha$ were generally negative except at the most negative angles of attack at the lower Mach numbers (fig. 17). The variations with angle of attack decreased as the Mach number increased. The ventral fin provided a negative contribution for angles of attack between -8° and $+8^\circ$.

The estimated values at zero and the low negative angles of attack were in fair agreement with the experimental results. Similar assumptions were made in predicting these values as in the case for $C_{l_r} - C_{l_{\dot{\beta}}} \cos \alpha$.

CONCLUSIONS

A flat-top wing-body configuration was tested in a supersonic air stream. From a consideration of the data, the following conclusions are drawn:

1. The model exhibited directional instability at most positive angles of attack.

2. There were pronounced cross-coupling effects with either elevon or rudder deflections upon the lateral and directional static stability of the model. With proper deflections of the rudder and elevons a pure yawing moment can be obtained; however, with deflections of these same surfaces, a pure rolling moment cannot be obtained.

3. The damping derivatives indicate stabilizing damping of the model at all angles of attack and Mach number.

4. The approximate methods of estimating the dynamic derivatives were only moderately successful and the predicted values of rolling moment due to yawing velocity were in poor agreement with the experimental results.

Ames Research Center
National Aeronautics and Space Administration
Moffett Field, Calif., Dec. 10, 1959

REFERENCES

1. Syvertson, Clarence A., Wong, Thomas J., and Gloria, Hermilo R.: Additional Experiments With Flat-Top Wing-Body Combinations at High Supersonic Speeds. NACA RM A56I11, 1957.

2. Migotsky, Eugene, and Adams, Gaynor J.: Some Properties of Wing and Half-Body Arrangements at Supersonic Speeds. NACA RM A57E15, 1957.

3. Eggers, A. J., Jr., and Syvertson, Clarence A.: Aircraft Configurations Developing High Lift-Drag Ratios at High Supersonic Speeds. NACA RM A55L05, 1956.

4. Huntsberger, Ralph F., and Parsons, John F.: The Design of Large High-Speed Wind Tunnels. Paper presented at Fourth General Assembly of the AGARD Wind Tunnel Panel at Scheveningen, The Netherlands, AG15/P6, May 3-7, 1954.

5. Beam, Benjamin H.: A Wind-Tunnel Test Technique for Measuring the Dynamic Rotary Stability Derivatives at Subsonic and Supersonic Speeds. NACA Rep. 1258, 1956. (Supersedes NACA TN 3347)

6. Ribner, Herbert S., and Malvestuto, Frank S., Jr.: Stability Derivatives of Triangular Wings at Supersonic Speeds. NACA Rep. 908, 1948. (Supersedes NACA TN 1572)

7. Brown, Clinton E., and Adams, Mac C.: Damping in Pitch and Roll of Triangular Wings at Supersonic Speeds. NACA Rep. 892, 1948. (Supersedes NACA TN 1566)

8. Allen, H. Julian, and Perkins, Edward W.: A Study of Effects of Viscosity on Flow Over Slender Inclined Bodies of Revolution. NACA Rep. 1048, 1951.

9. Tobak, Murray, Reese, David E., Jr., and Beam, Benjamin H.: Experimental Damping in Pitch of 45° Triangular Wings. NACA RM A50J26, 1950.

TABLE I.- INDEX OF FIGURES

Subject	Figure
Static longitudinal characteristics	
C_L vs. α, C_D, C_m; $\beta = 0^\circ$	4
β vs. C_L, C_D, C_m; $\alpha = 6^\circ$	5
α vs. C_{m_α}; $\beta = 0^\circ$	6
α vs. $\Delta C_m/\Delta\delta_e$; $\beta = 0^\circ$	7
Dynamic longitudinal characteristics	
α vs. $C_{m_q} + C_{m_{\dot\alpha}}$	8
Static lateral-directional characteristics	
α vs. C_n, C_l, C_Y; $\beta = 0^\circ$	9
β vs. C_n, C_l, C_Y; $\alpha = 6^\circ$	10
α vs. $\Delta C_n/\Delta\beta$, $\Delta C_l/\Delta\beta$; $\beta = 0^\circ$	11
α vs. $\Delta C_n/\Delta\delta$, $\Delta C_l/\Delta\delta$; $\beta = 0^\circ$	12
α vs. C_{n_β}; $\beta = 0^\circ$	13
Dynamic lateral-directional characteristics	
α vs. $C_{n_r} - C_{n_{\dot\beta}} \cos\alpha$; $\beta = 0^\circ$	14
α vs. $C_{l_r} - C_{l_{\dot\beta}} \cos\alpha$; $\beta = 0^\circ$	15
α vs. $C_{l_p} + C_{l_{\dot\beta}} \sin\alpha$; $\beta = 0^\circ$	16
α vs. $C_{n_p} + C_{n_{\dot\beta}} \sin\alpha$; $\beta = 0^\circ$	17

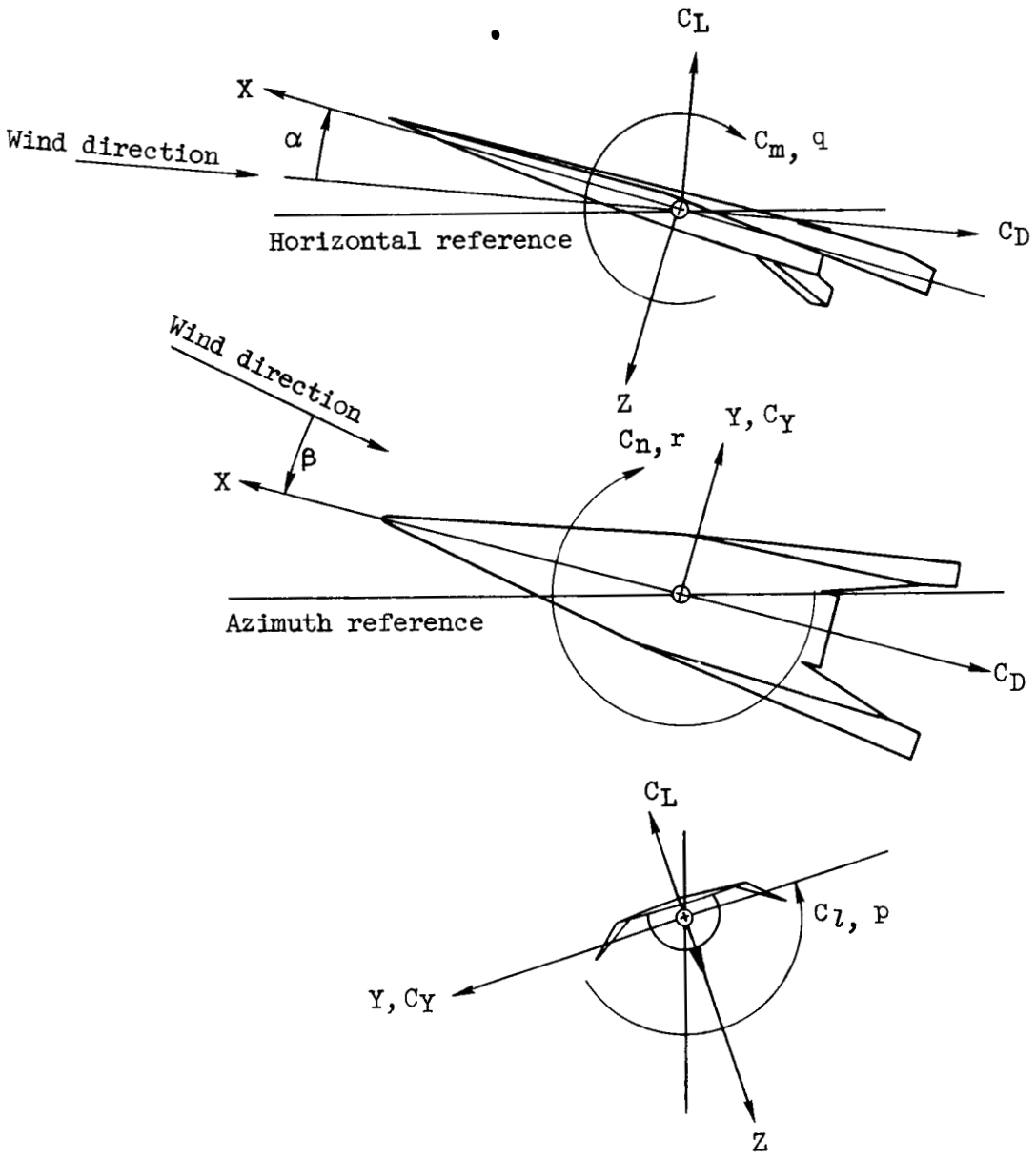

Figure 1.- The body axis system showing the positive direction of forces, moments, and motions when $\alpha \approx 0°$.

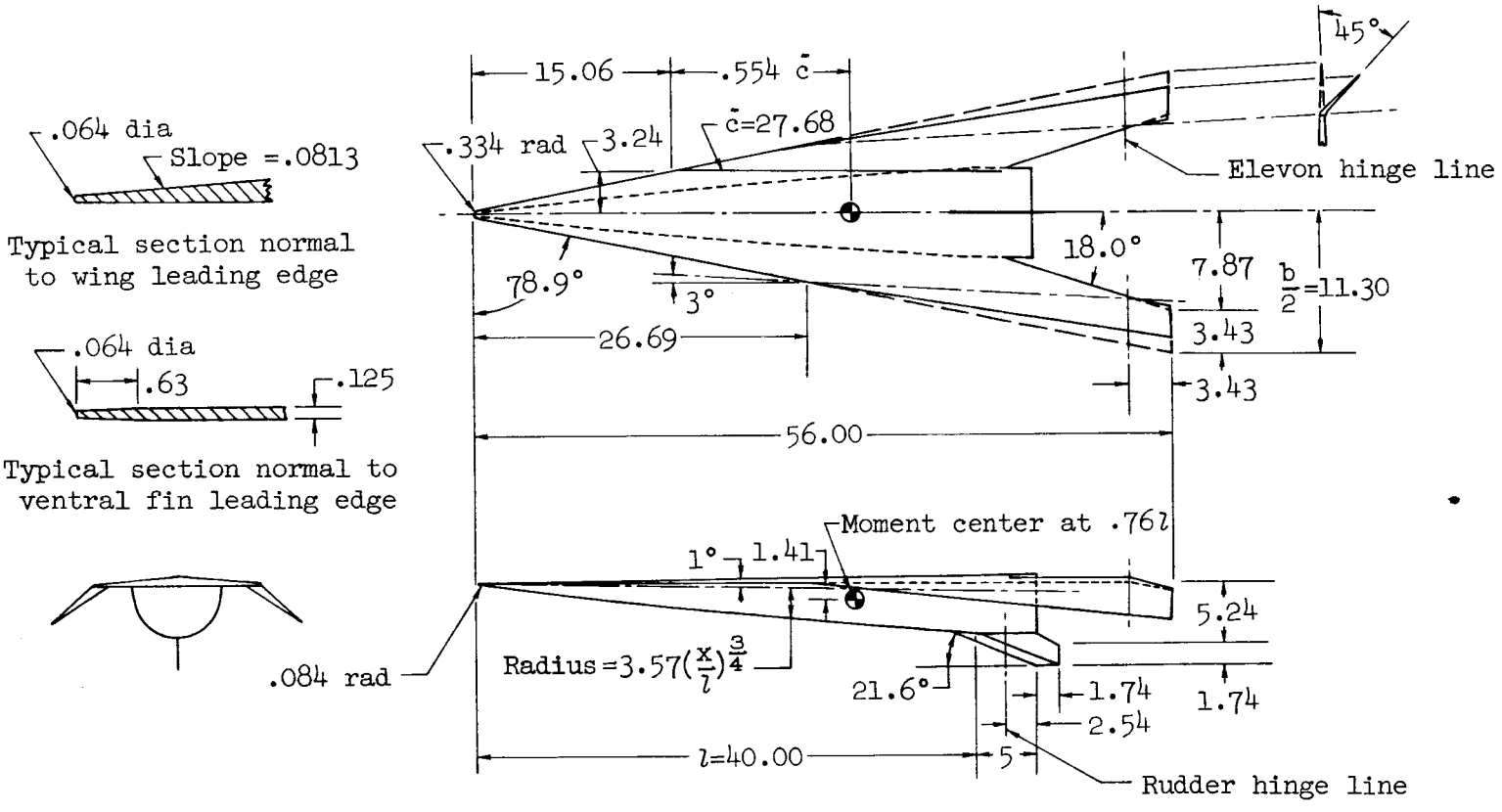

Figure 2.- Geometry and dimensions of test model. Dimensions are given in inches.

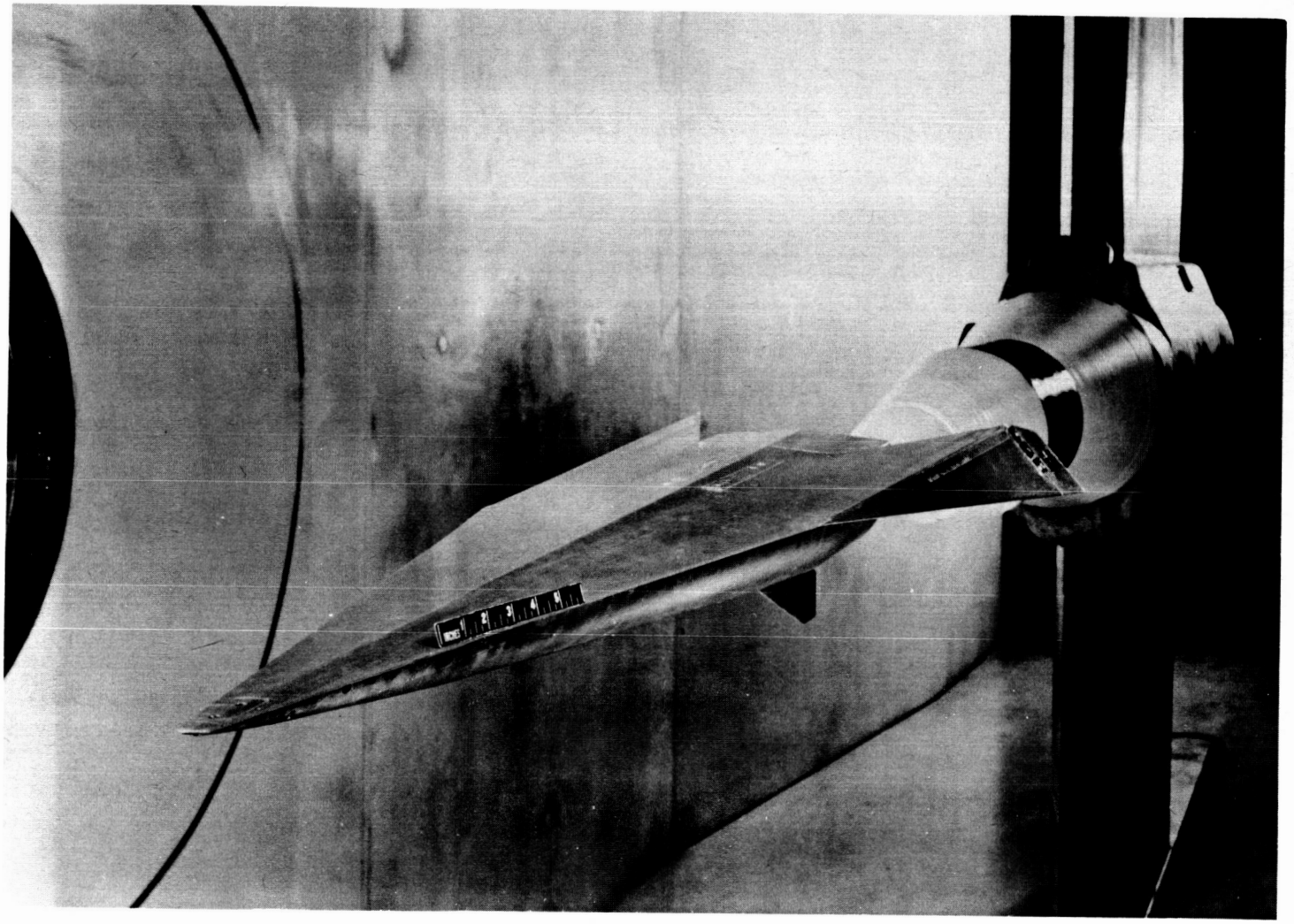

A-23326

(a) Three-quarter front view.

Figure 3.- Photograph of the model mounted on the sting in the wind-tunnel test section.

CONFIDENTIAL

A-23451

(b) Three-quarter rear view.

Figure 3.- Concluded.

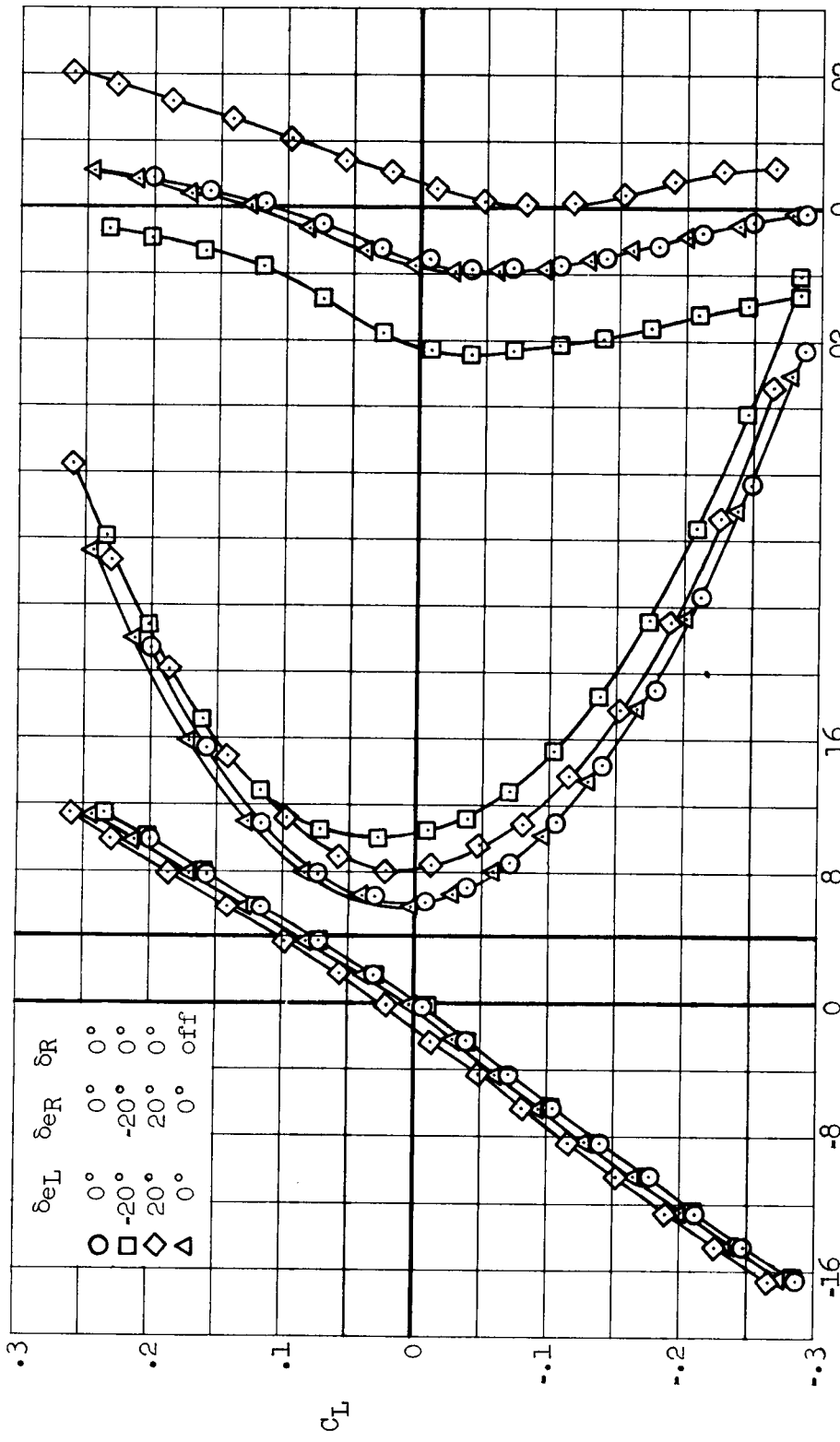

(a) M = 2.5

Figure 4.- Longitudinal characteristics at β = 0°.

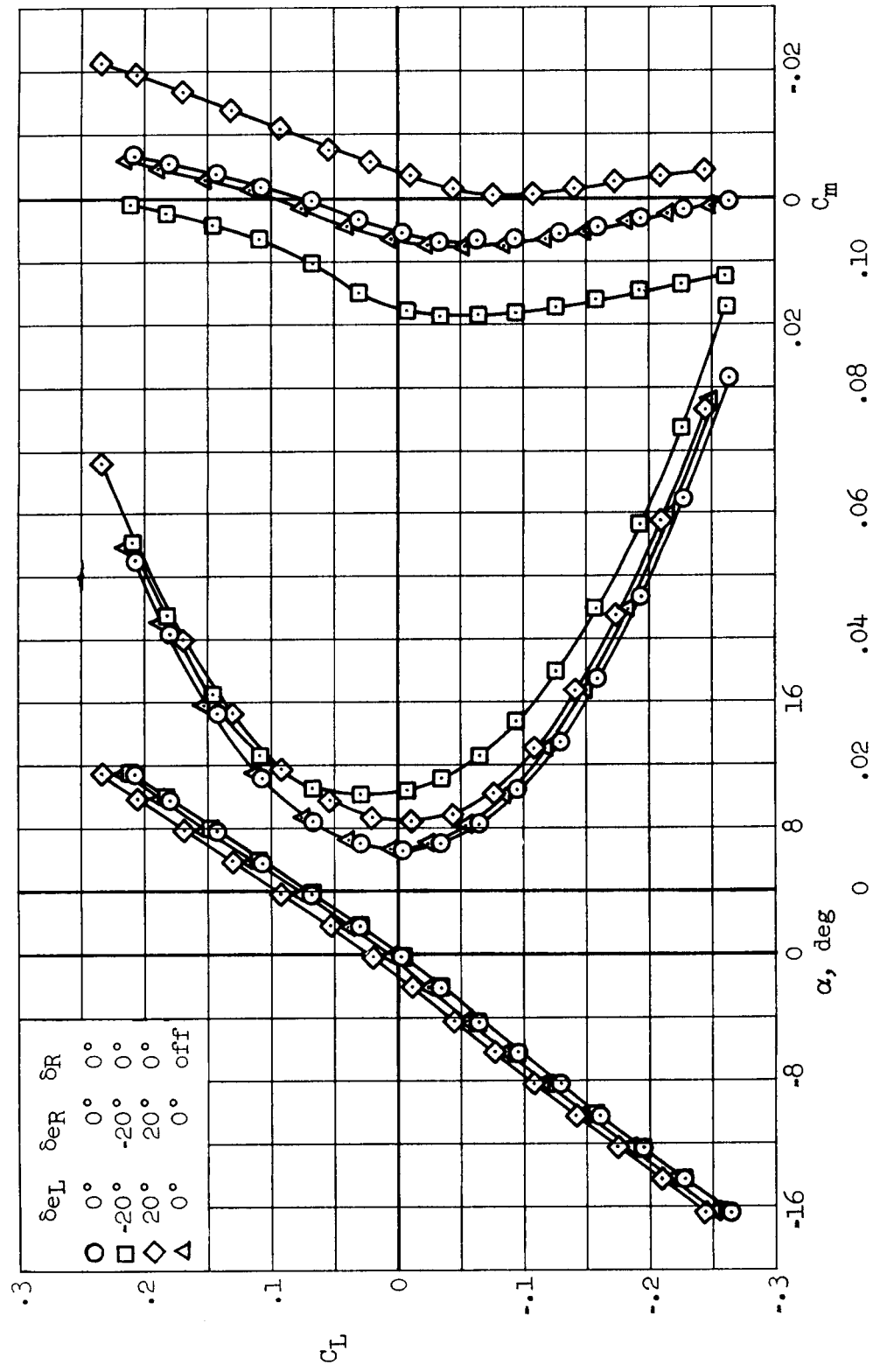

(b) M = 3.0

Figure 4.- Continued.

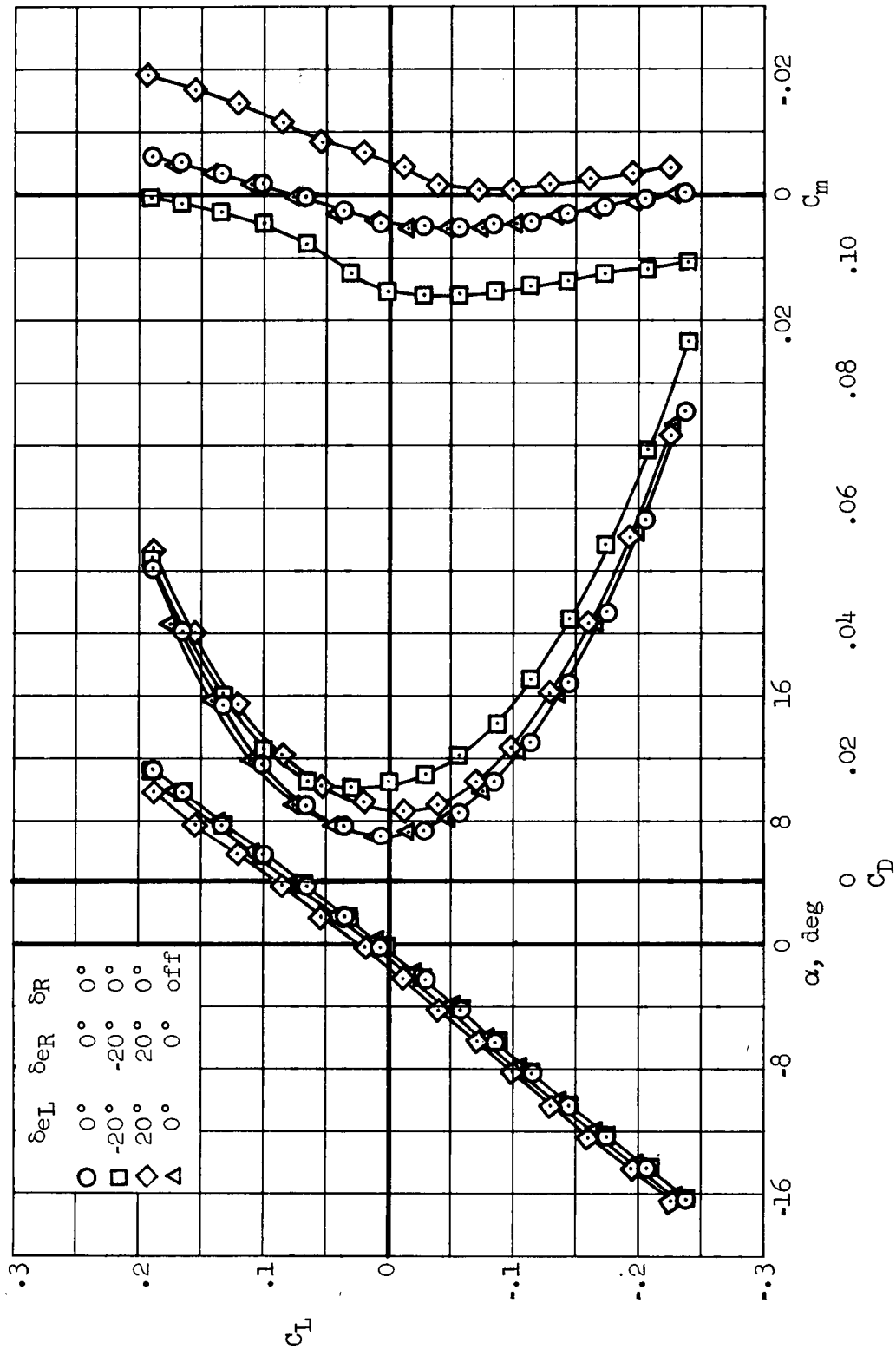

(c) M = 3.5

Figure 4.- Concluded.

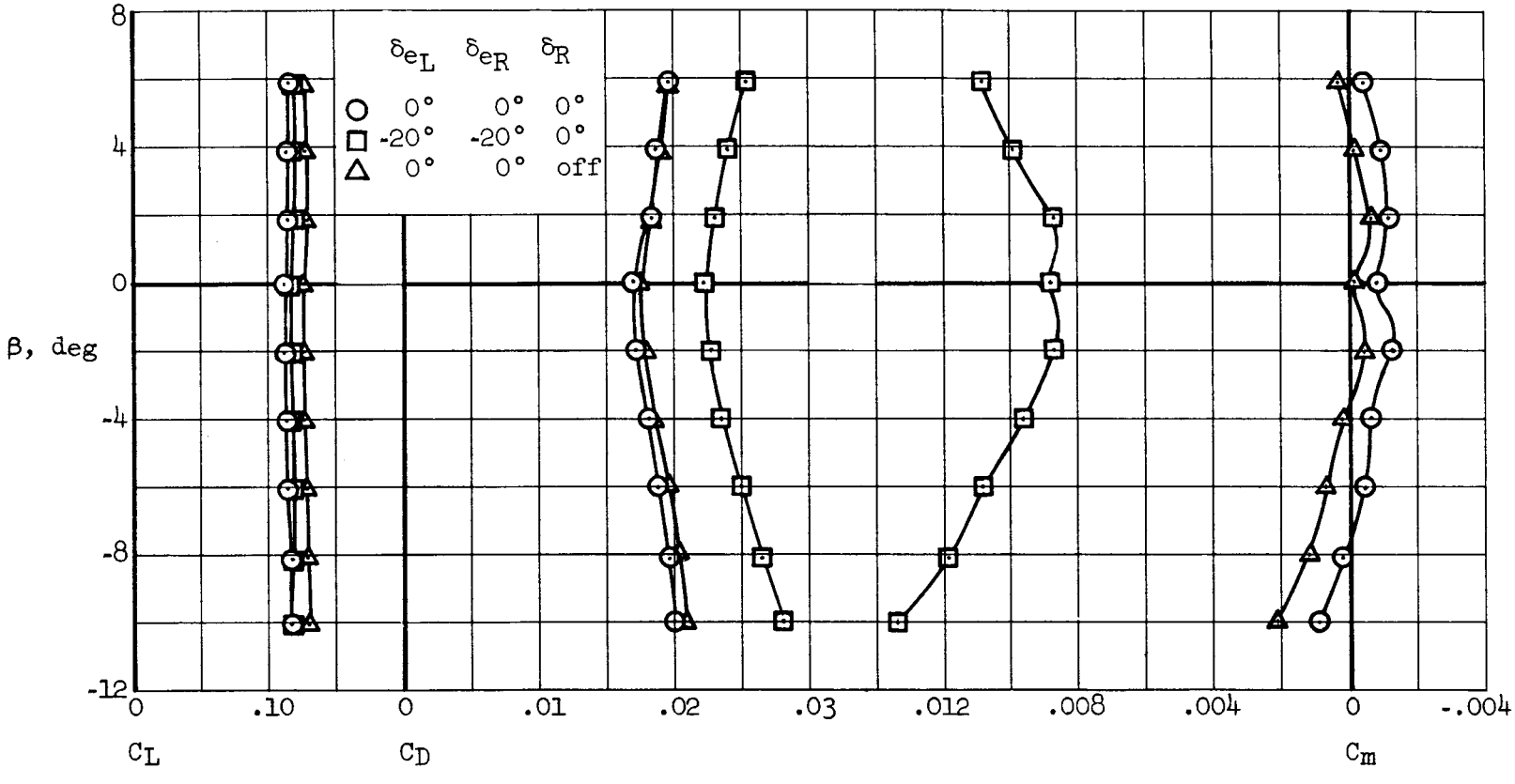

(a) M = 2.5

Figure 5.- Longitudinal characteristics in sideslip at $\alpha = 6°$.

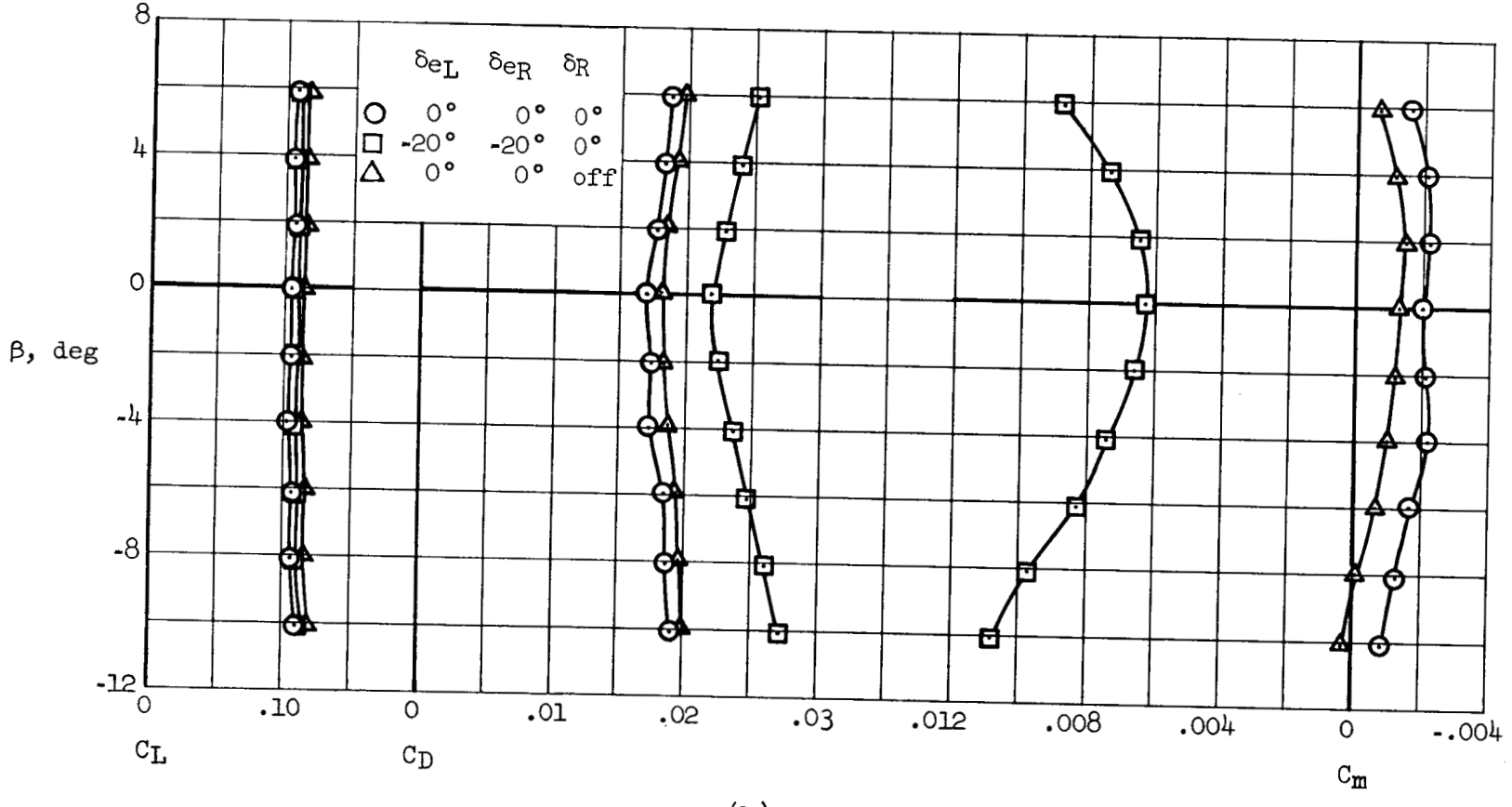

(b) M = 3.0

Figure 5.- Continued.

CONFIDENTIAL

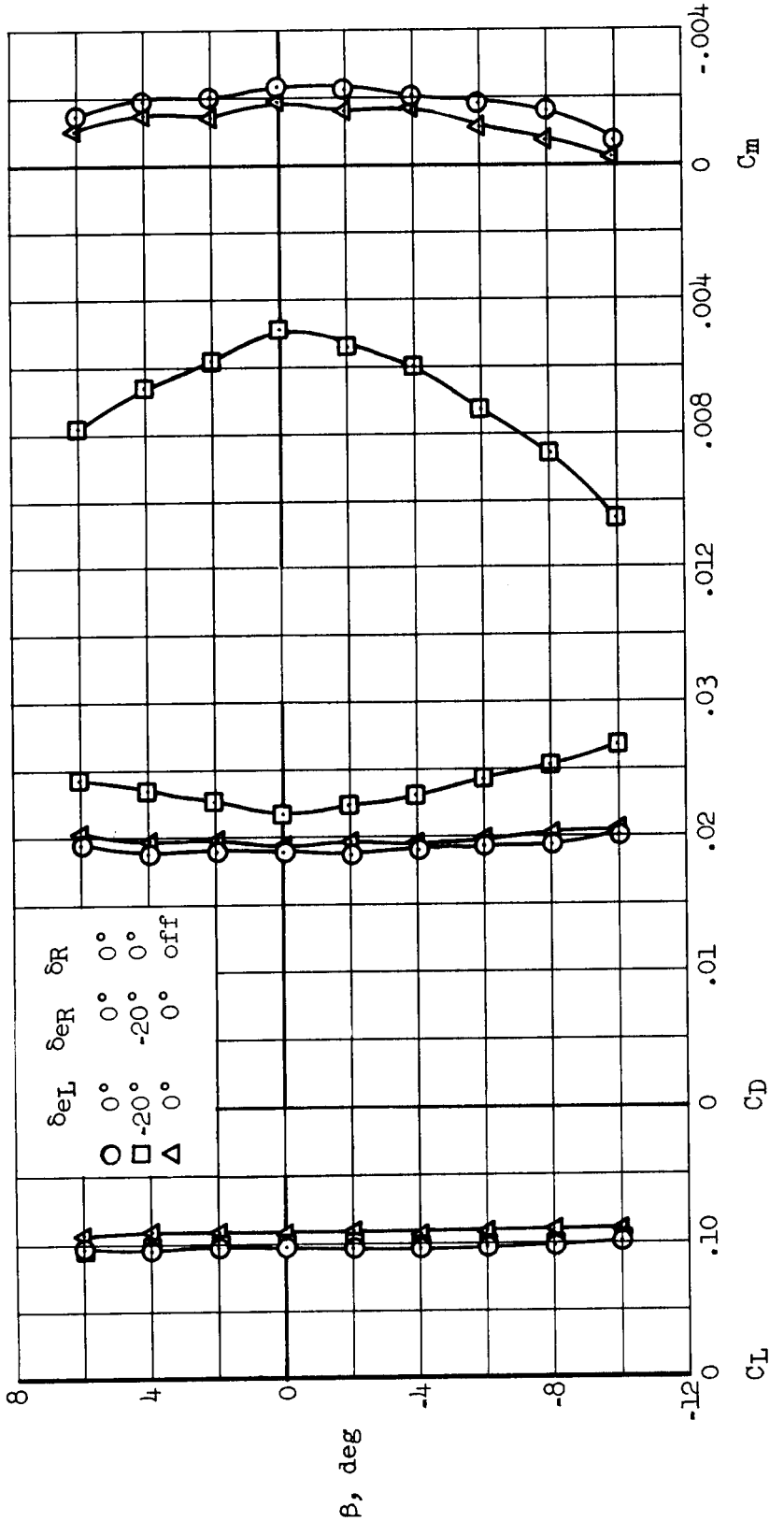

(c) M = 3.5

Figure 5.- Concluded.

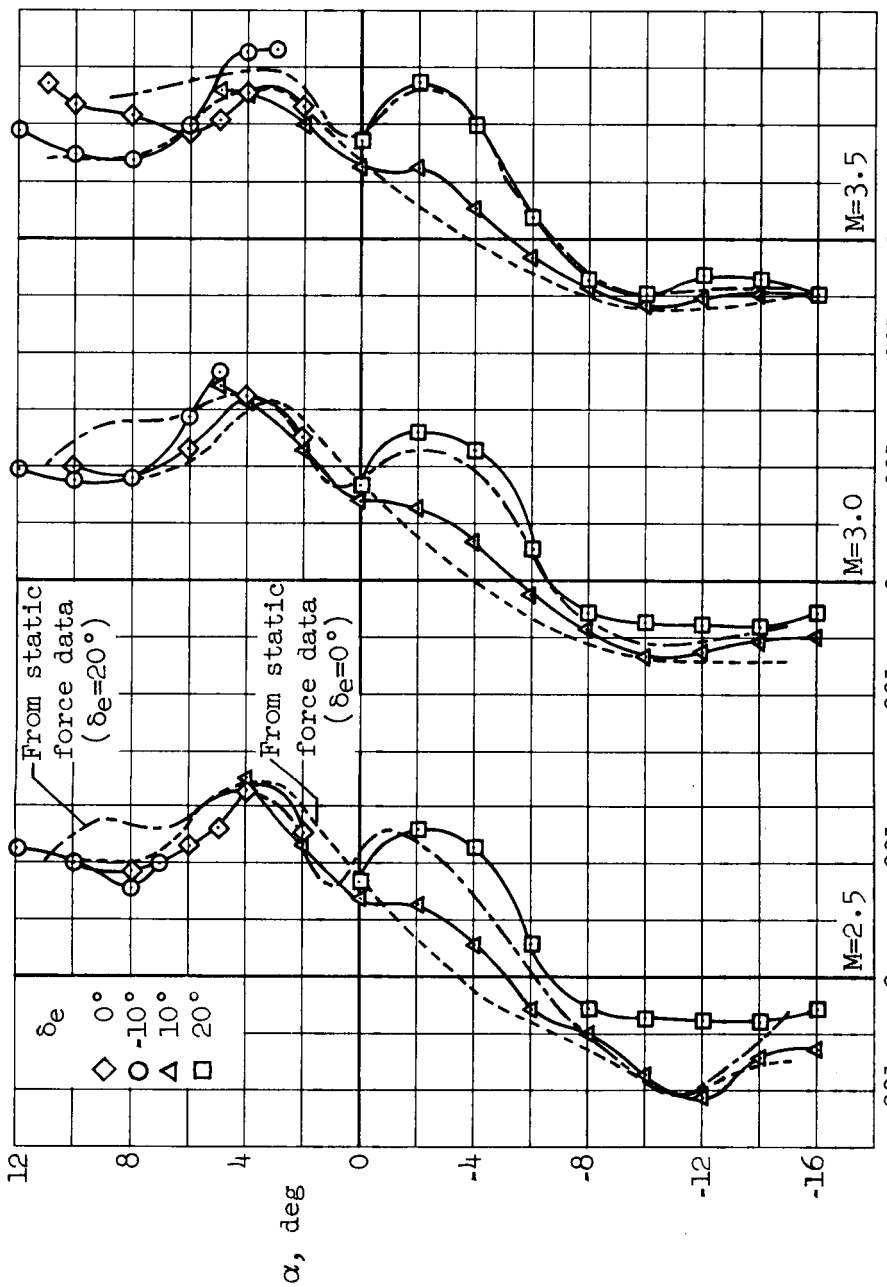

Figure 6.- The variation with angle of attack of the longitudinal pitching derivative as measured with the dynamic balance.

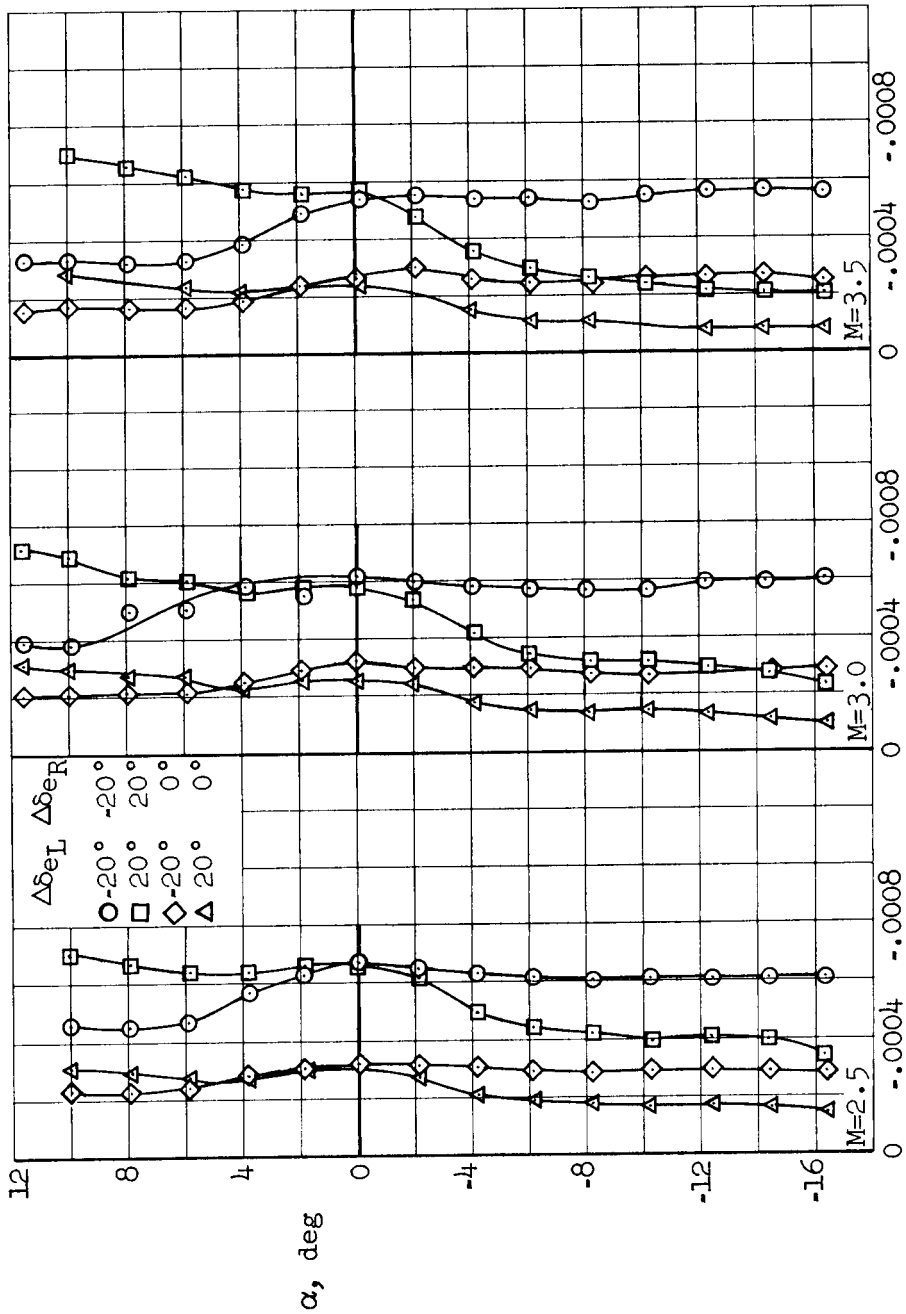

Figure 7.- The variation of elevon pitch effectiveness with angle of attack at $\beta = 0°$.

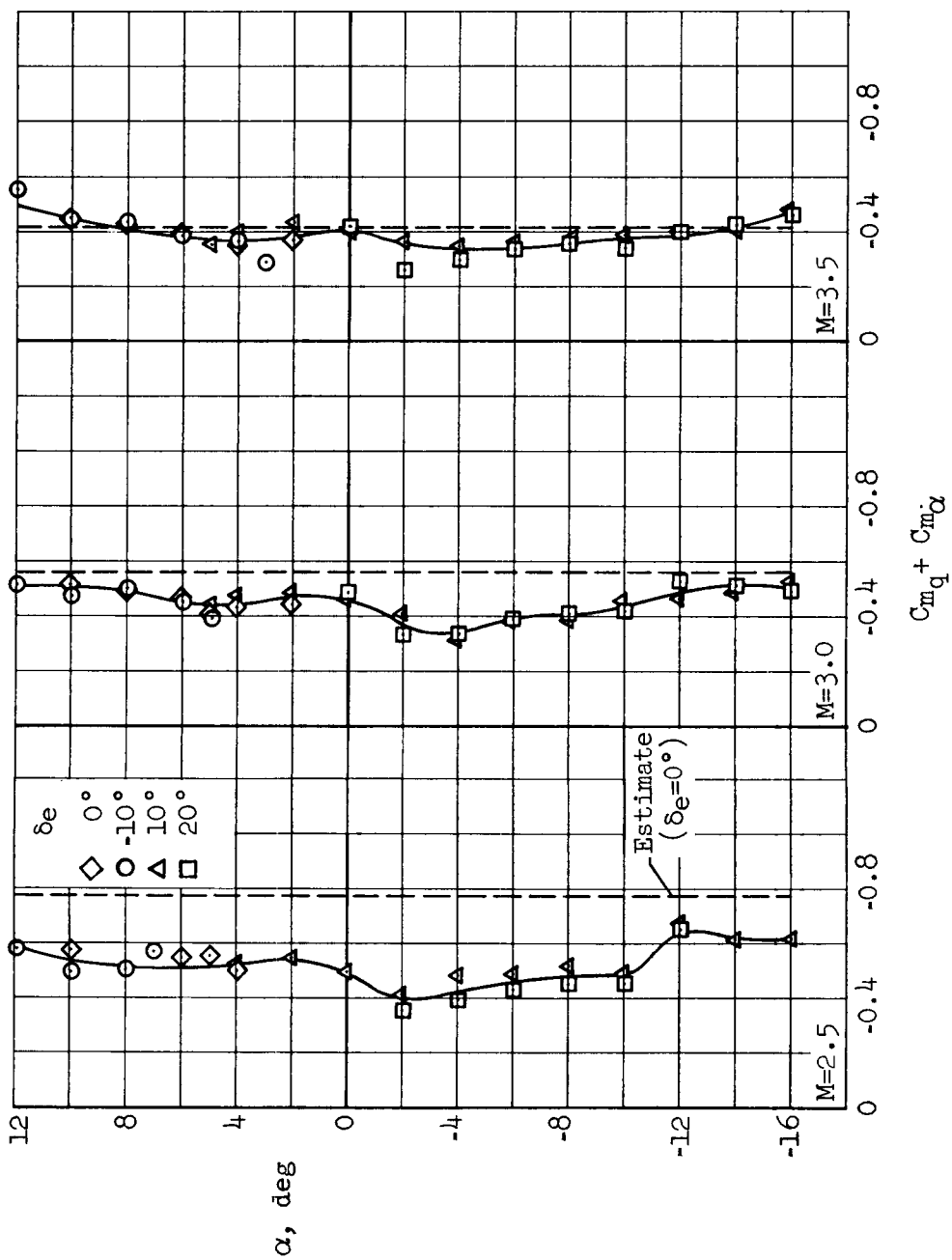

Figure 8.- The variation with angle of attack of the damping in pitch stability derivative.

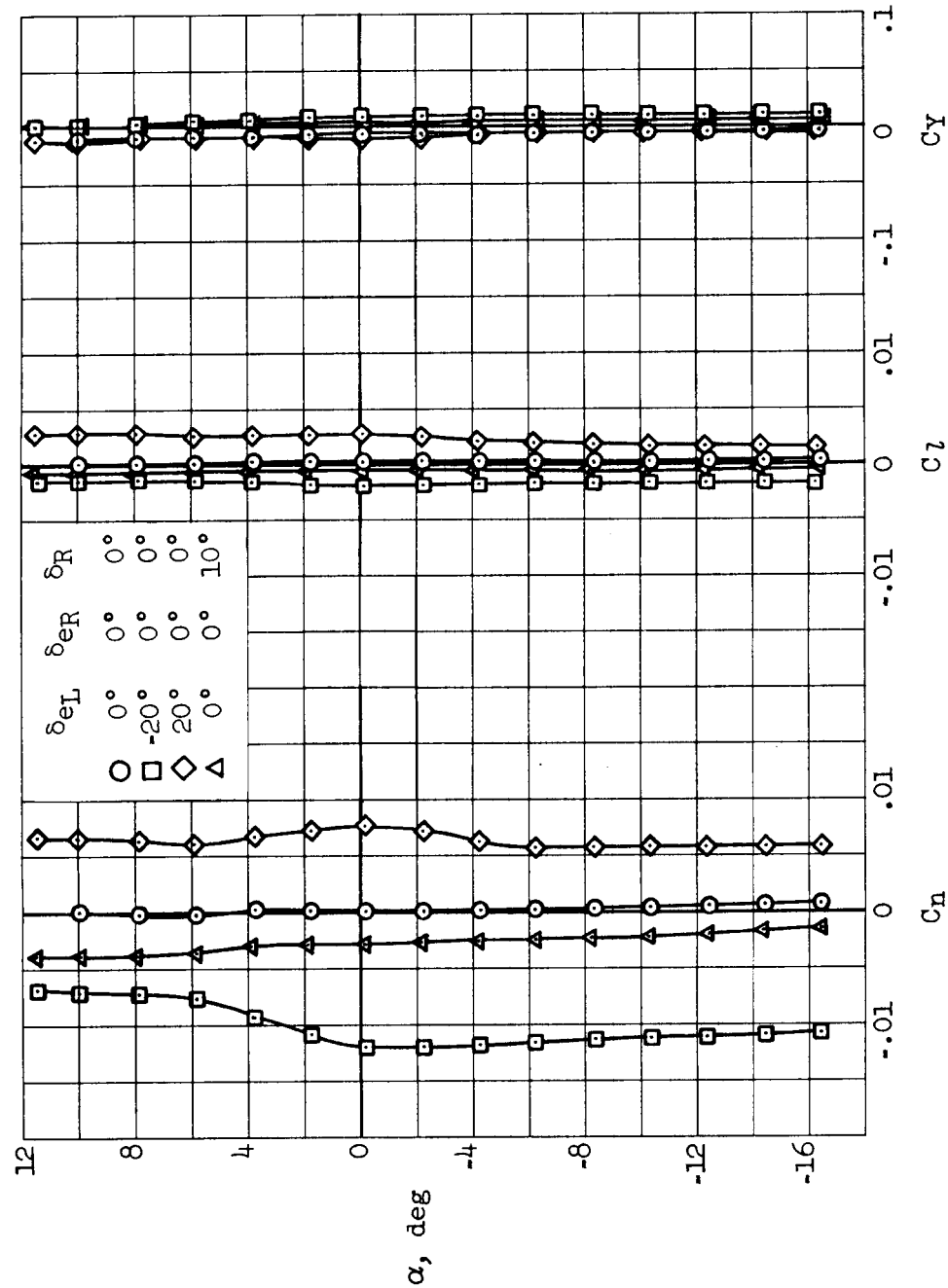

(a) M = 2.5

Figure 9.- Lateral and directional characteristics at β = 0°.

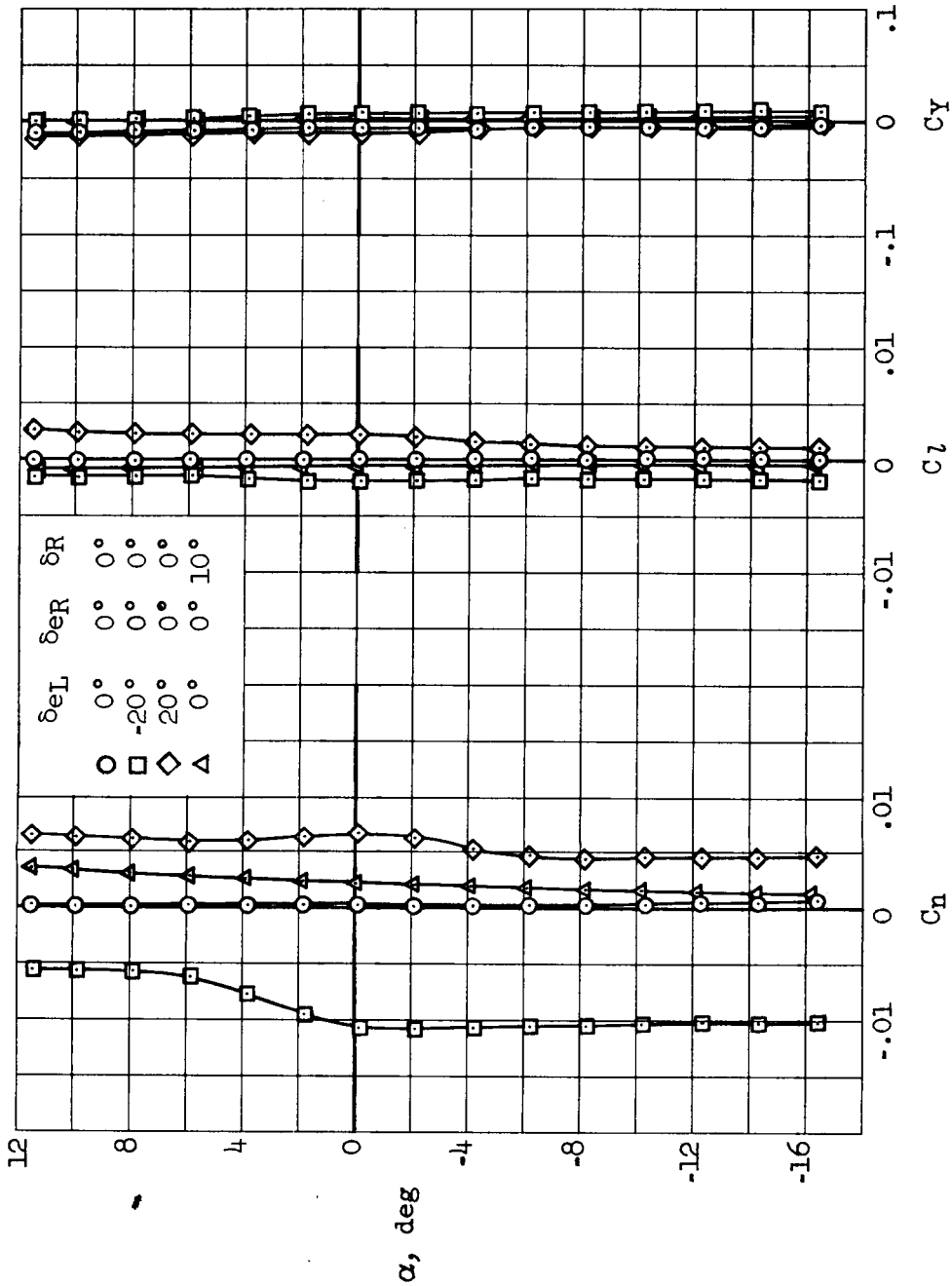

(b) M = 3.0

Figure 9.- Continued.

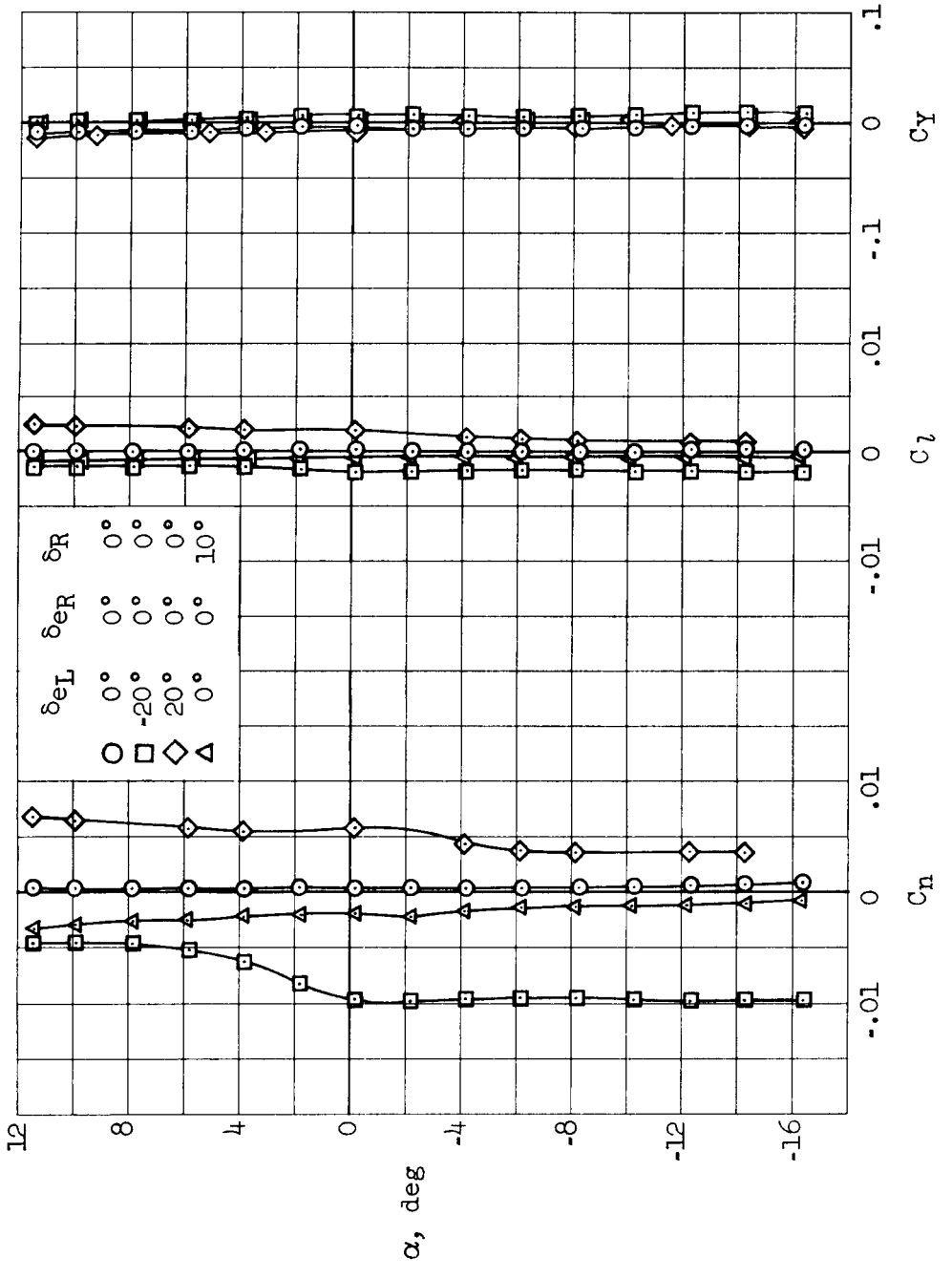

(c) M = 3.5

Figure 9.- Concluded.

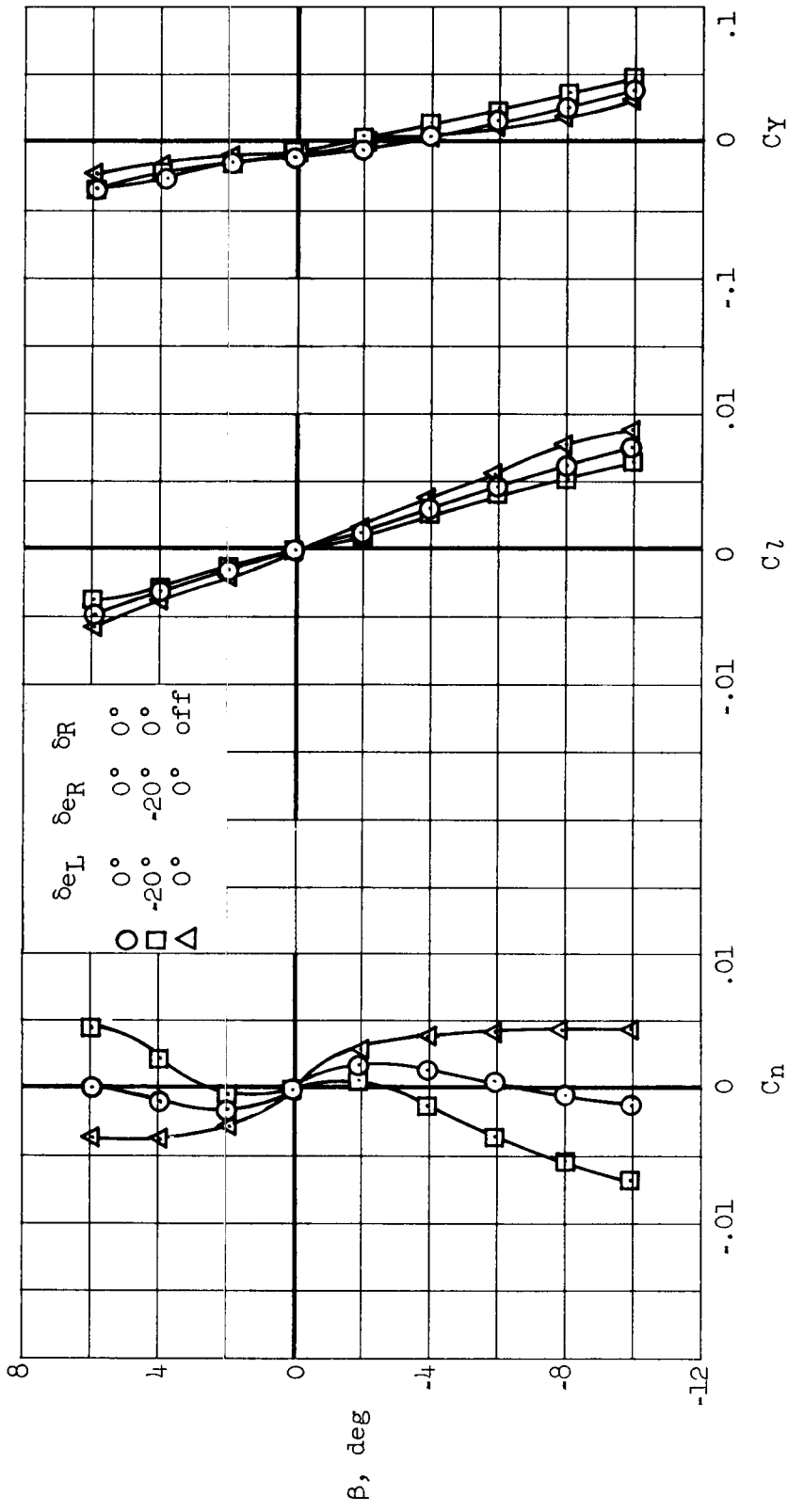

(a) M = 2.5

Figure 10.- Lateral and directional characteristics in sideslip at $\alpha = 6°$.

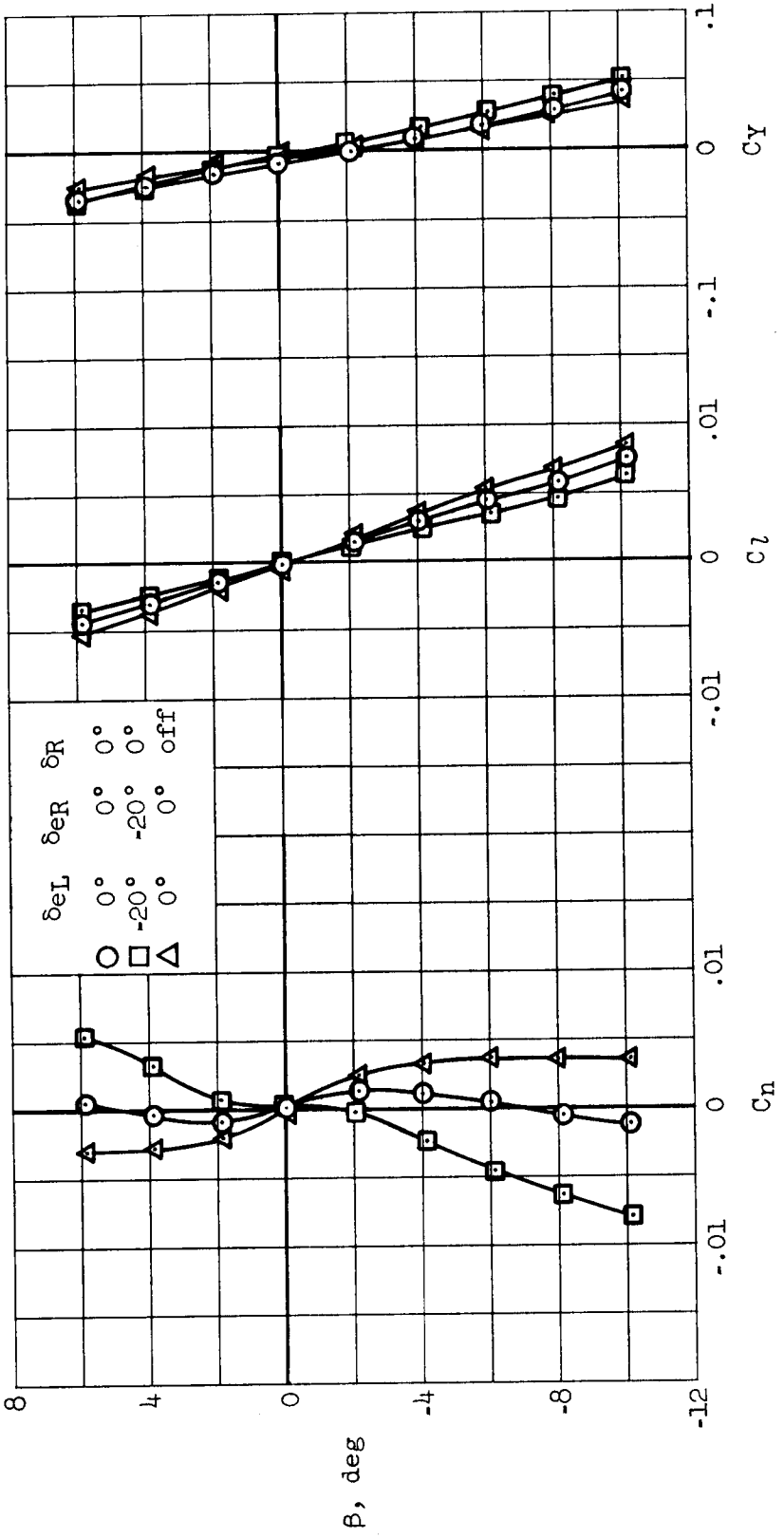

(b) M = 3.0

Figure 10.- Continued.

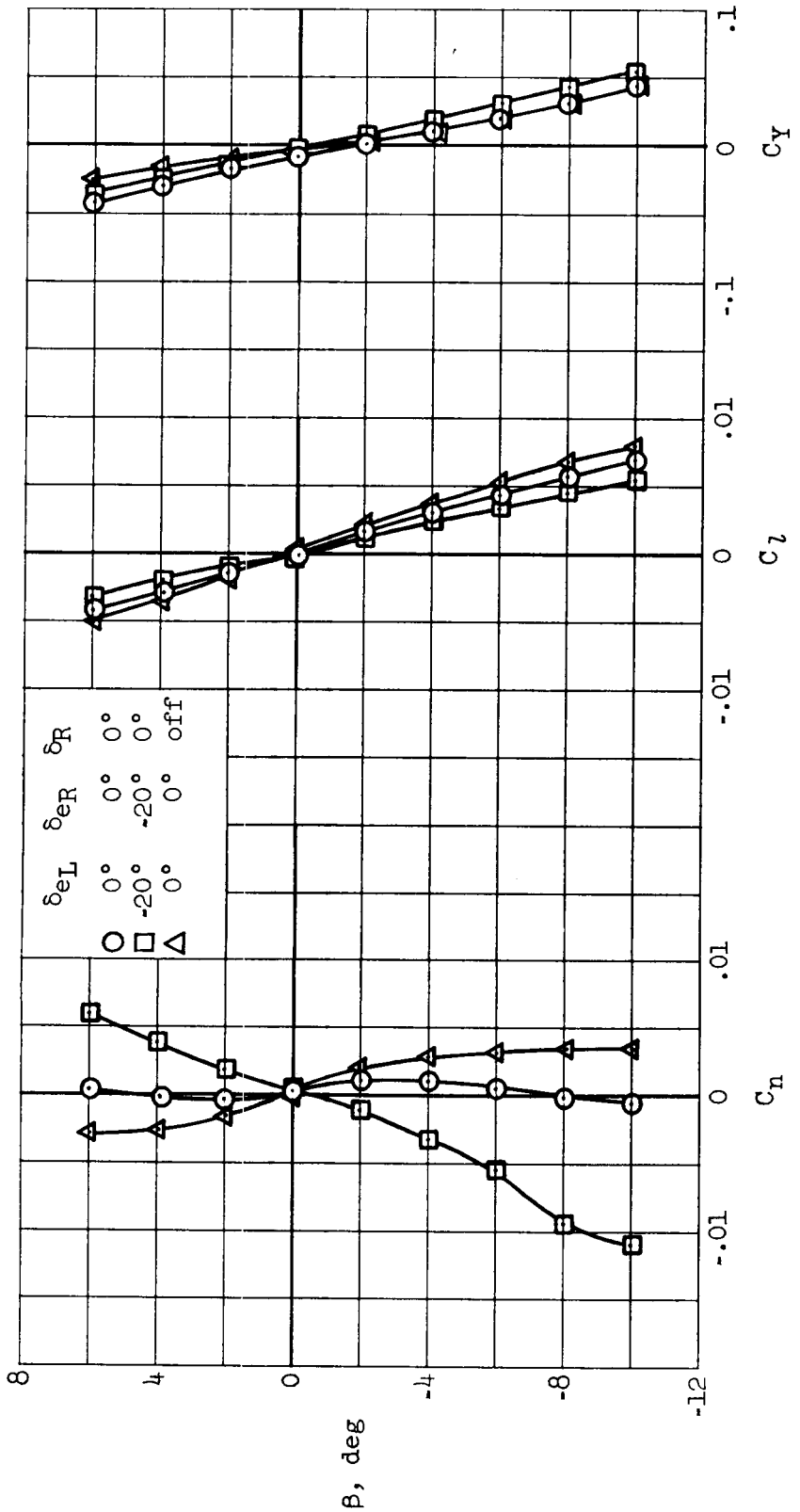

(c) M = 3.5

Figure 10.- Concluded.

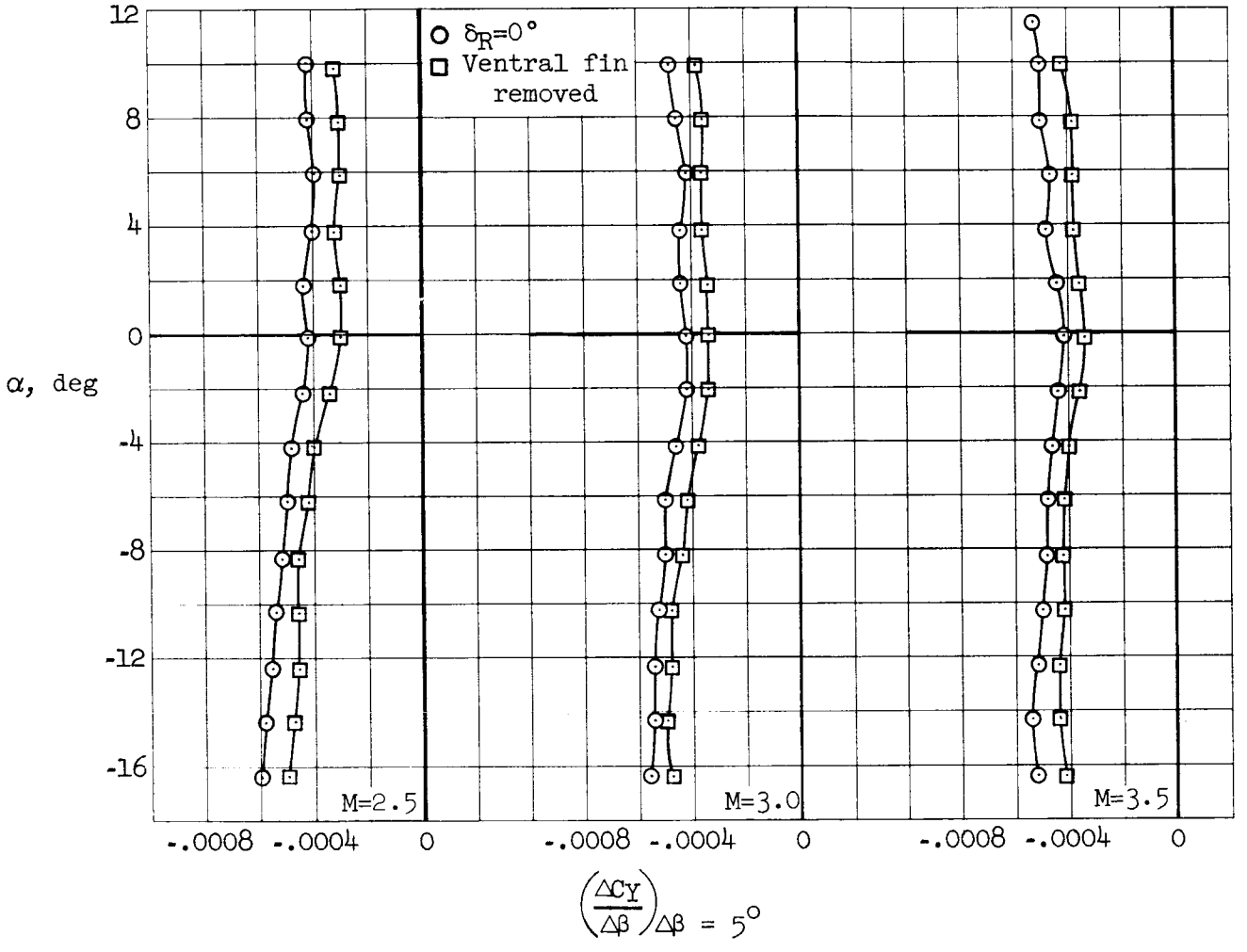

(a) Side force

Figure 11.- The variation of the lateral and directional stability derivatives with angle of attack from six-component-balance data.

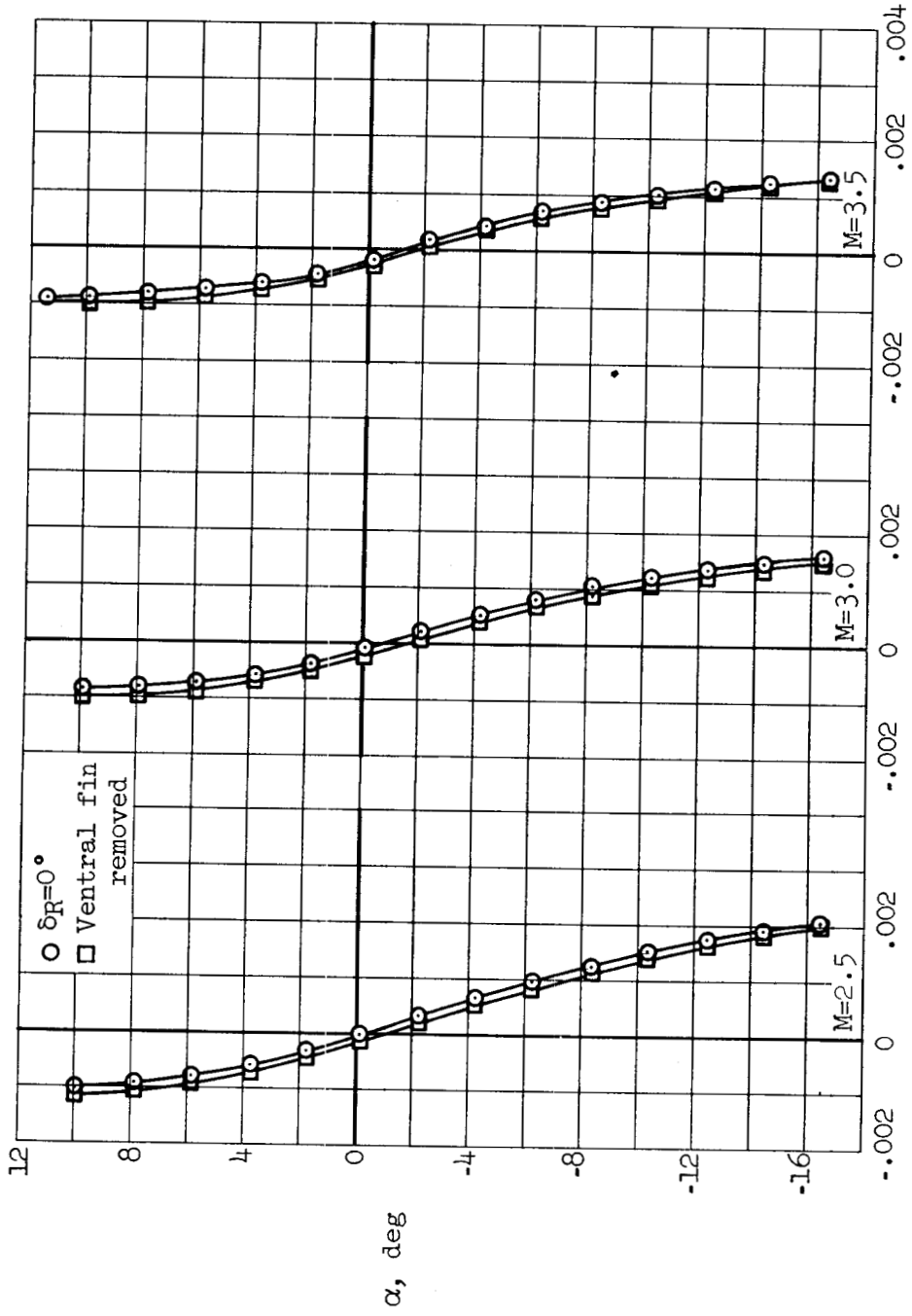

(b) Rolling moment

Figure 11.- Continued.

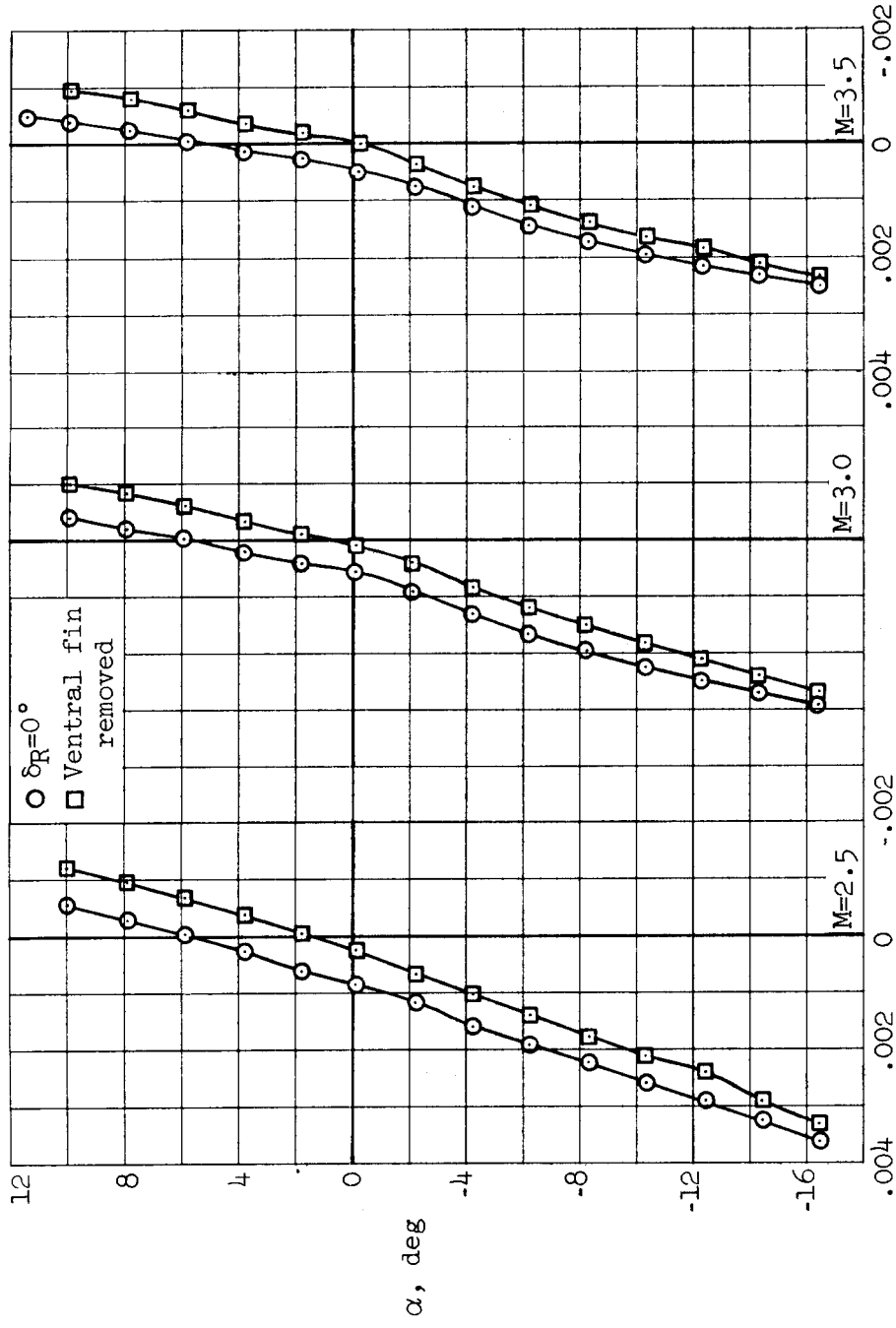

(c) Yawing moment

Figure 11.- Concluded.

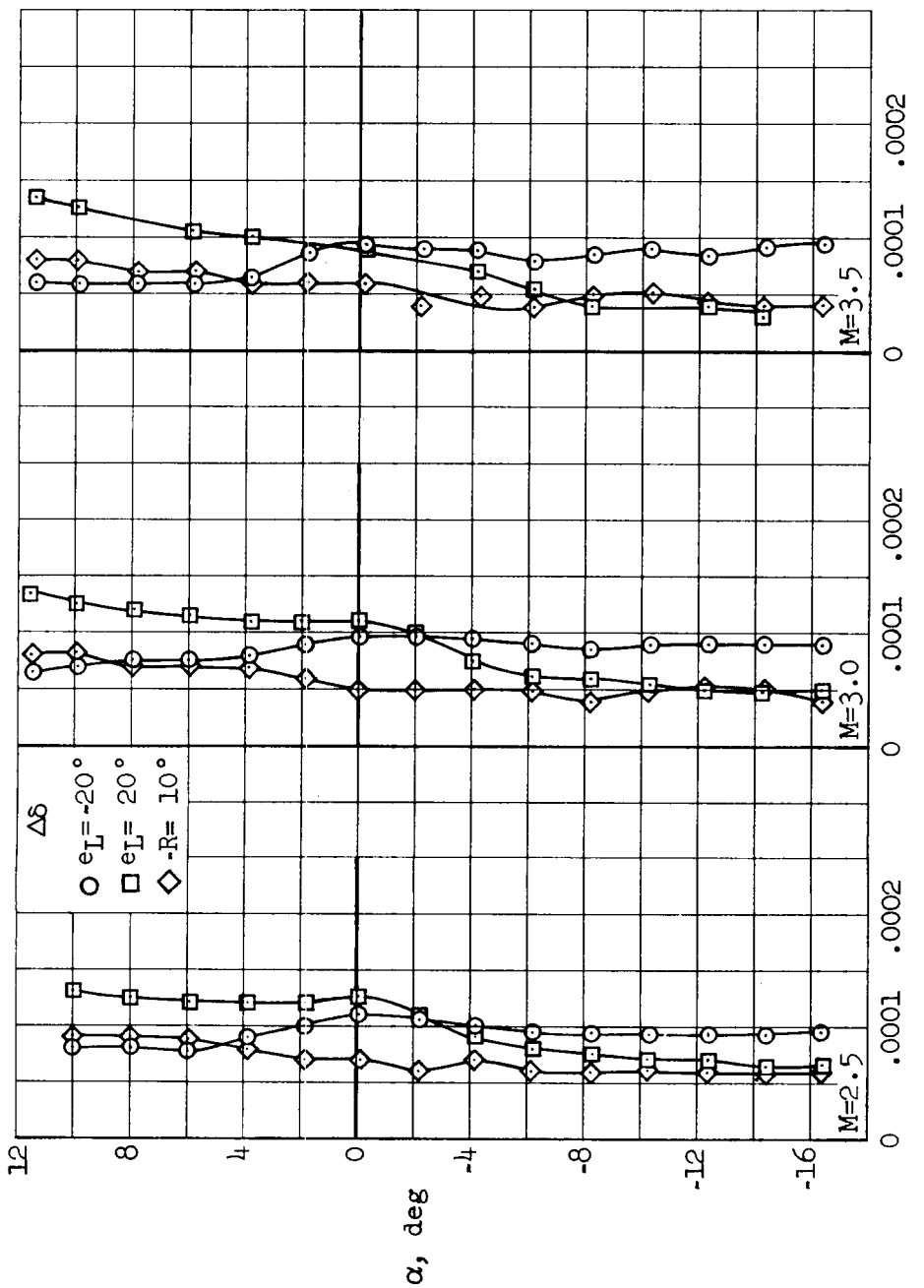

(a) Rolling effectiveness.

Figure 12.- Rudder and single elevon effectiveness.

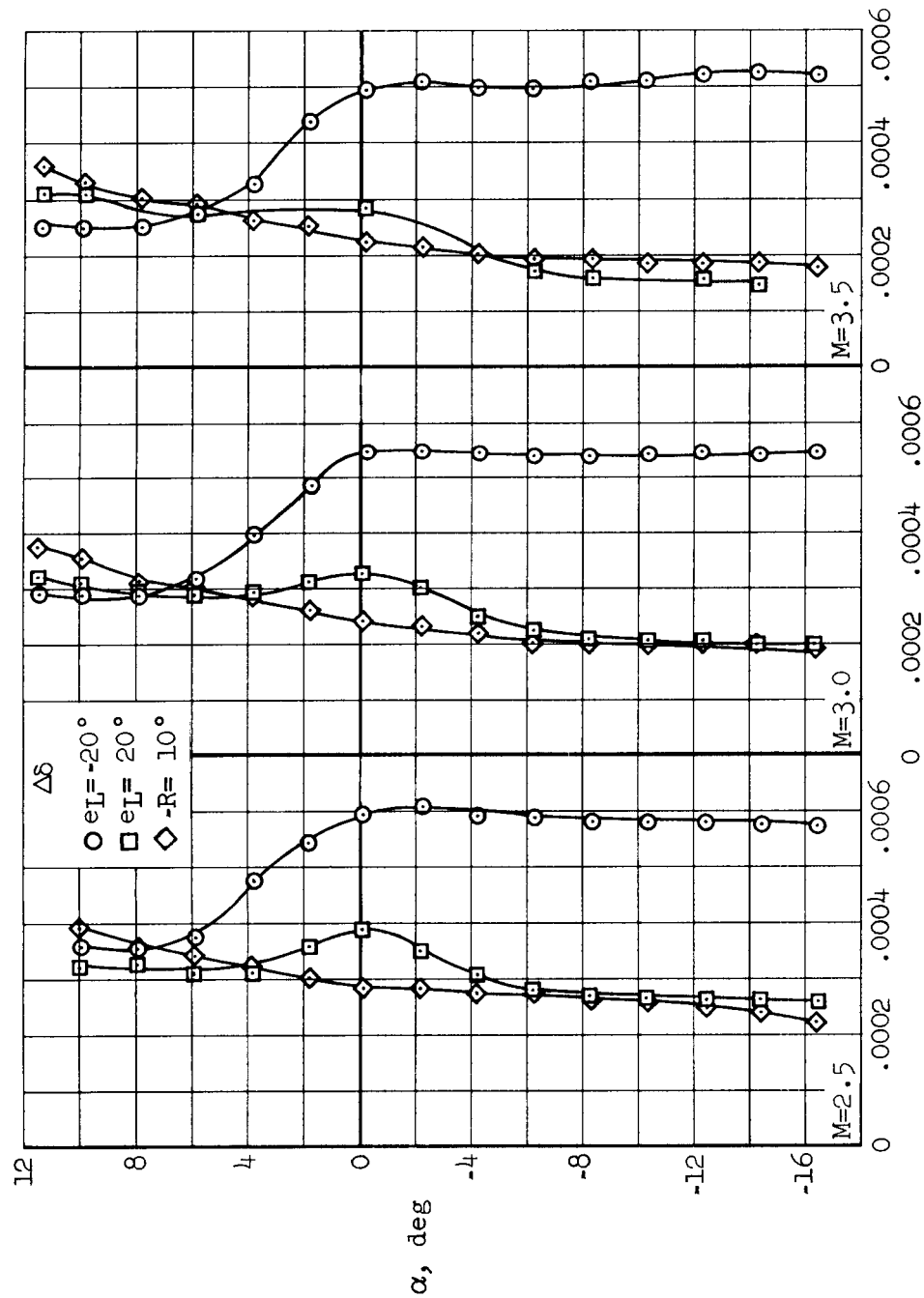

(b) Yawing effectiveness

Figure 12.- Concluded.

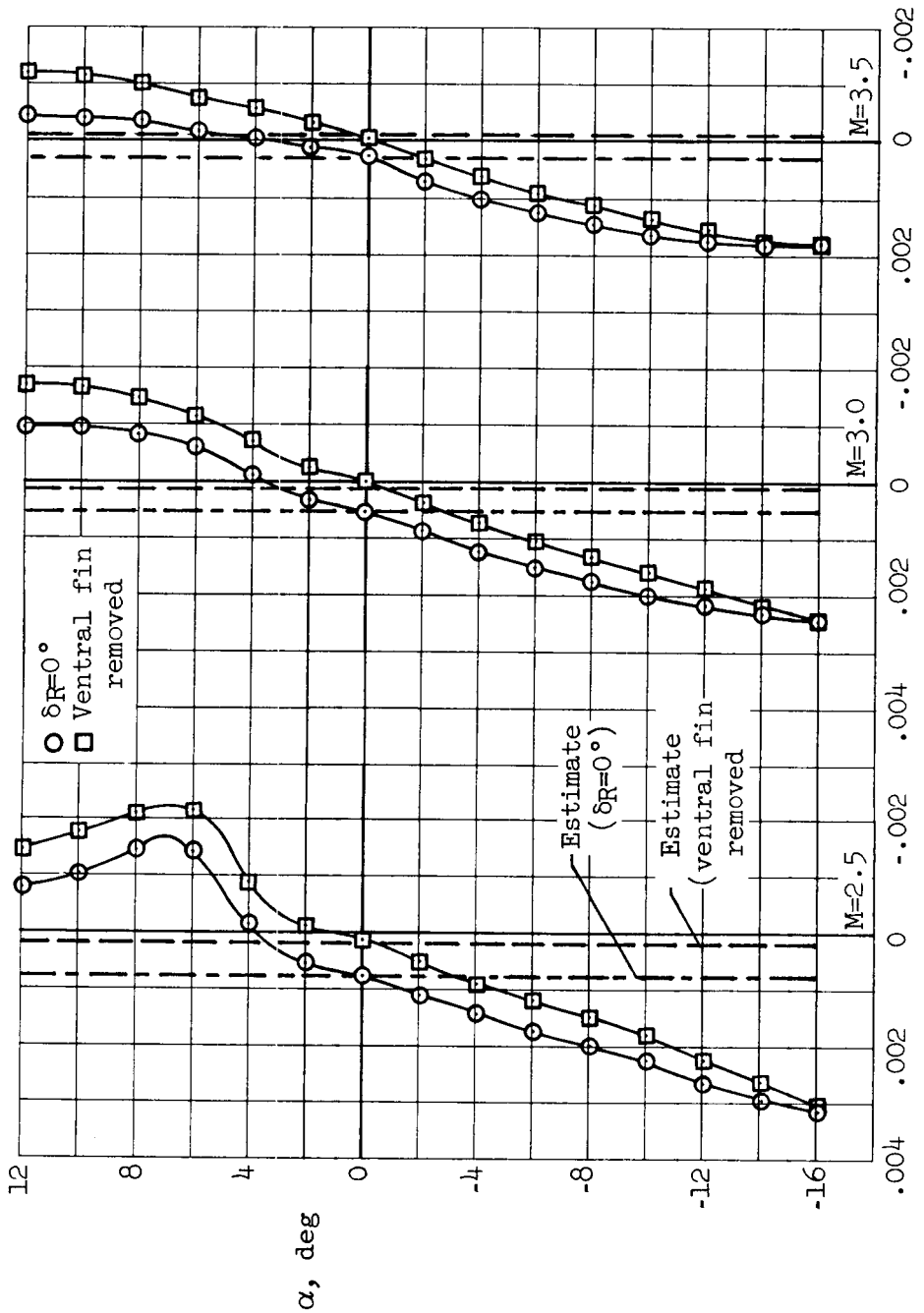

Figure 13.- The variation with angle of attack of the static directional stability derivative as measured with the dynamic balance.

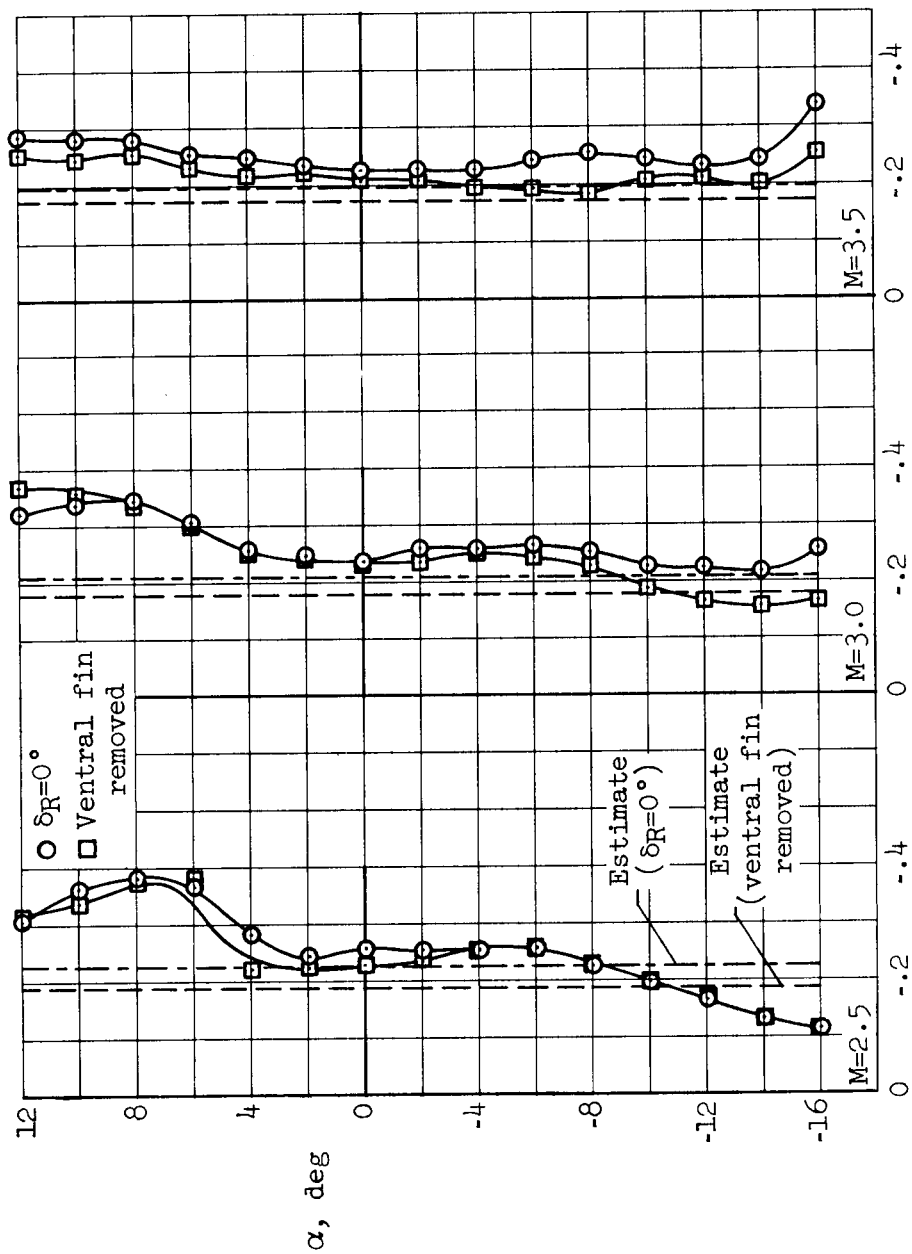

Figure 14.- The variation with angle of attack of the damping in yaw stability derivative.

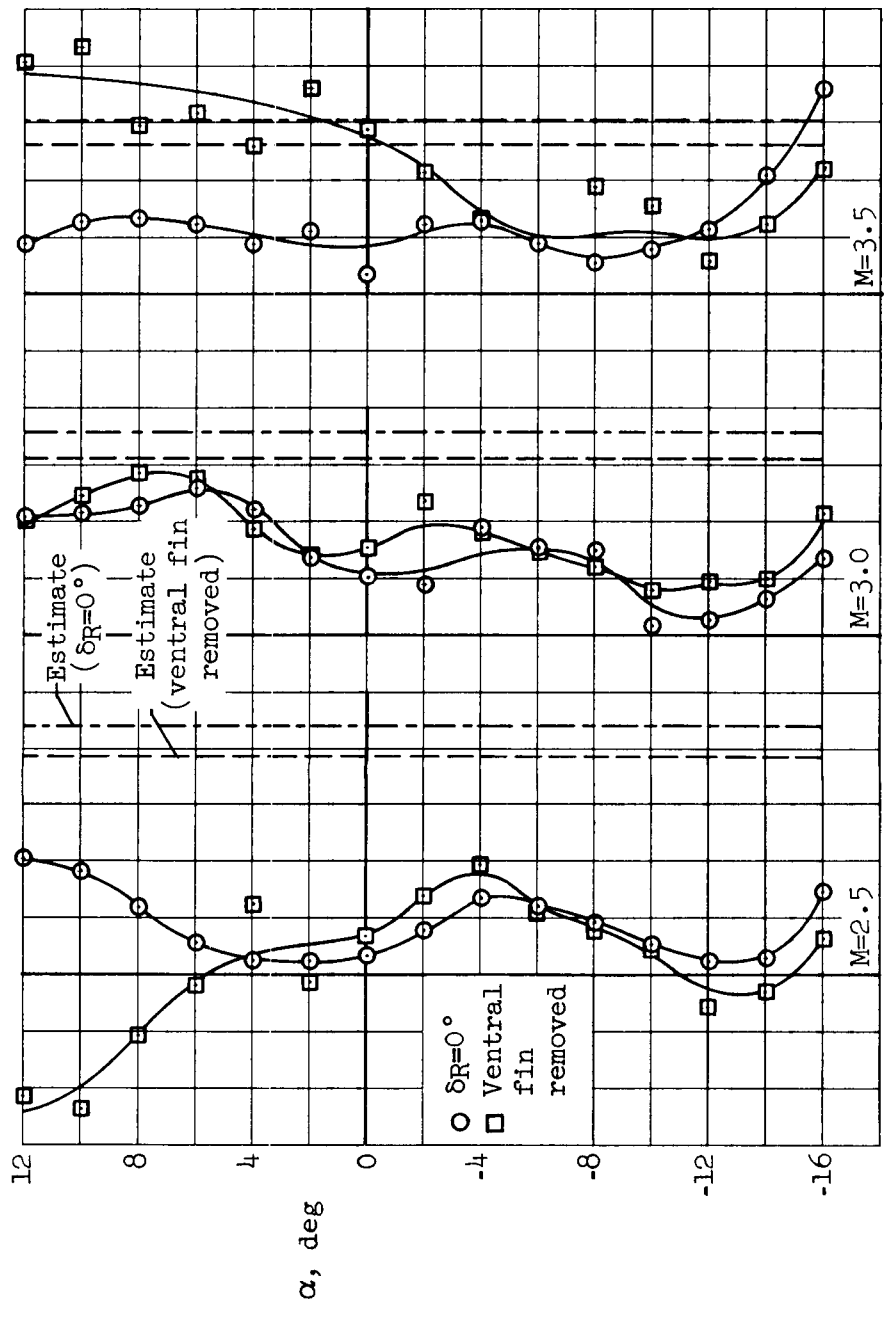

Figure 15.- The variation with angle of attack of the rolling moment due to yawing velocity stablity derivative.

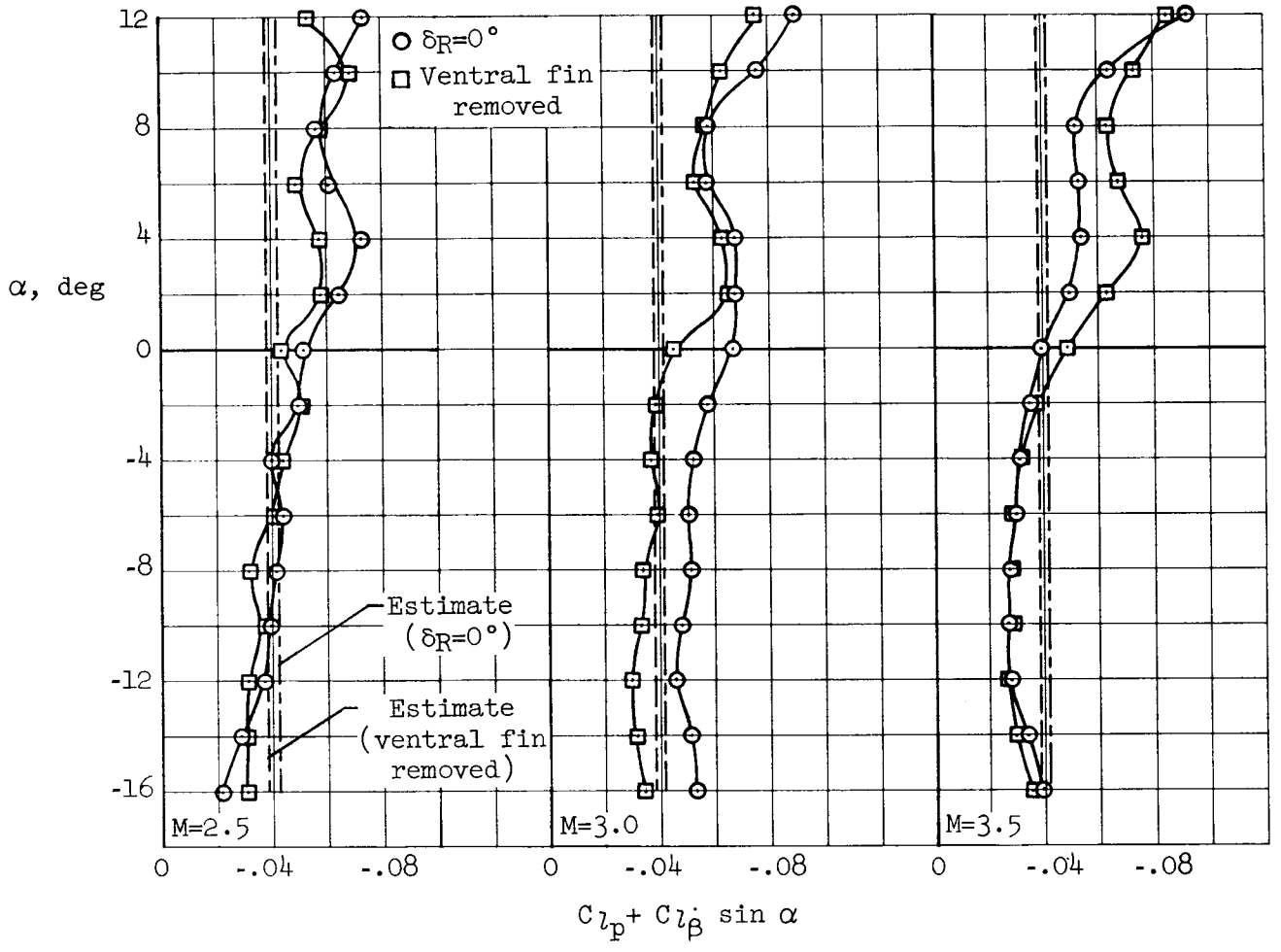

Figure 16.- The variation with angle of attack of the damping in roll stability derivative.

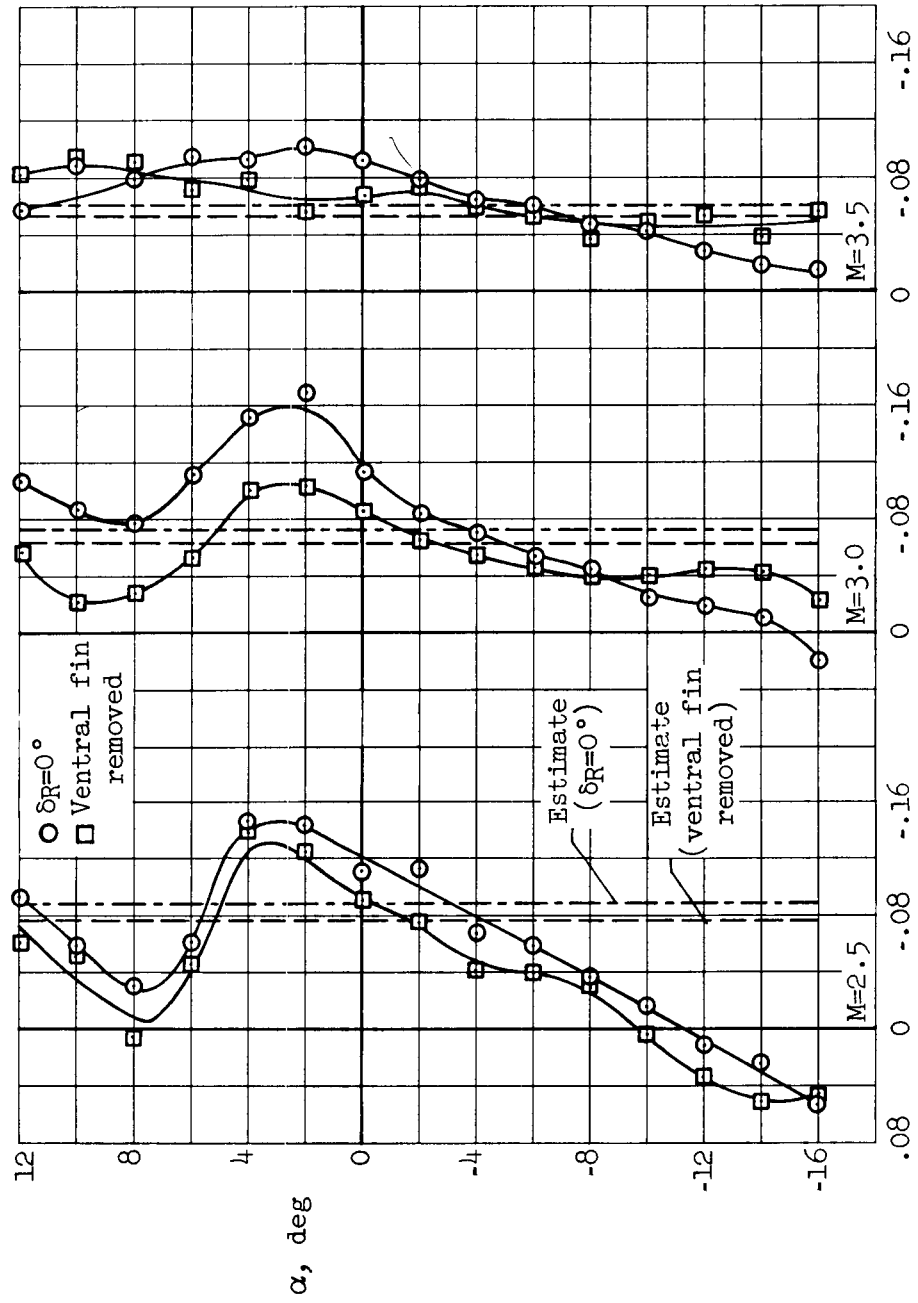

Figure 17.- The variation with angle of attack of the yawing-moment-due-to-rolling-velocity stability derivative.

NASA - Langley Field, Va. A-208